



# A family of Multiscale Hybrid-Mixed finite element methods for the Darcy equation with rough coefficients



Christopher Harder<sup>1</sup>, Diego Paredes<sup>2</sup>, Frédéric Valentin <sup>\*,1</sup>

Applied Mathematics Department, National Laboratory for Scientific Computing – LNCC, Av. Getúlio Vargas, 333 25651-070 Petrópolis, RJ, Brazil

## ARTICLE INFO

### Article history:

Received 3 August 2011

Received in revised form 3 March 2013

Accepted 4 March 2013

Available online 26 March 2013

### Keywords:

Elliptic equation

Darcy model

Mixed method

Hybrid method

Finite element

Rough coefficient

## ABSTRACT

We aim at proposing novel stable finite element methods for the mixed Darcy equation with heterogeneous coefficients within a space splitting framework. We start from the primal hybrid formulation of the elliptic model for the pressure. Localization of this infinite-dimensional problem leads to element-level boundary value problems which embed multiscale and high-contrast features in a natural way, with Neumann boundary conditions driven by the Lagrange multipliers. Such a procedure leads to methods involving the space of piecewise constants for the pressure together with a discretization of the fluxes. Choosing (arbitrarily) polynomial interpolations, the lowest-order Raviart–Thomas element as well as some recent multiscale methods are recovered. In addition, the methods assure local mass conservation and can be interpreted as stabilized primal hybrid methods. Extensive numerical validation attests to the accuracy of the new methods on academic and more realistic problems with rough coefficients.

© 2013 Elsevier Inc. All rights reserved.

## 1. Introduction

The numerical simulation of fluid flows in porous media, as found in saline aquifers or petroleum reservoirs, is of fundamental importance when it comes to managing water resources or oil extraction. Regarding the latter, the nature of the fluid inside the reservoir strongly depends on the current stage of oil recovery [13]. Primary recovery is usually modeled through a single phase flow, whereas secondary recovery uses a two-phase immiscible flow to account for the injection of water into some wells. However, inefficiencies arising from saturation during secondary recovery have lead engineers to seek miscibility by injecting CO<sub>2</sub> gas, thereby enhancing oil recovery [33]. Recently, this strategy has attracted particular attention as a reservoir may be seen as a storage site to sequester the gas indefinitely, with possible benefits for the environment.

Each stage of oil recovery is driven by distinct sets of differential partial equations. Among them is the mixed form of the Darcy equation with highly heterogeneous coefficients, which takes part in all modeling stages and is responsible for establishing the velocity of the fluid through a linear relationship with the pressure gradient. The Darcy model may also be interpreted as the mixed form of the Laplace equation with a modified right-hand side.

As a result of its mixed form, the numerical resolution of the Darcy equation by finite element methods requires the discrete spaces satisfy an inf-sup (or compatibility) condition [10]. Examples of stable pairs of interpolation spaces for the Darcy equation have been available since the seventies [30]. Notable examples among them are the family of RT (Raviart–Thomas), BDM (Brezzi–Douglas–Marini), and BDDM (Brezzi–Douglas–Duran–Marini) elements (see [10] for details). As a consequence

\* Corresponding author. Tel.: +55 24 22336082.

E-mail addresses: [harder@lncc.br](mailto:harder@lncc.br) (C. Harder), [dparedes@lncc.br](mailto:dparedes@lncc.br) (D. Paredes), [valentin@lncc.br](mailto:valentin@lncc.br) (F. Valentin).

<sup>1</sup> The authors are supported by CNPq/Brazil.

<sup>2</sup> The author is supported by CONICYT/Chile.

of using discontinuous polynomial basis functions for both pressure and velocity variables, as well as face degrees of freedom for the velocity, these methods produce a locally conservative velocity with continuous normal components across faces.

On the other hand, the accuracy of the method may seriously deteriorate when the solution presents multiscale or high-contrast behavior due to heterogeneous coefficients. Such an issue, first addressed in [6] for the one-dimensional elliptic problem, led to the concept of generalized basis functions, and has since been addressed by different research groups [4,12,35]. Overall, these works focus on perturbing stable pairs of interpolation spaces in order to incorporate multiscale or high-contrast aspects of the problem. Although the approach differs among them, they share the strategy of incorporating such features through the solution of element-wise local problems. Therefore, it is not surprising that some relationship between the different methods has been demonstrated. For instance, the Petrov–Galerkin enriched (PGEM) [7,23,8,22,1] and the residual-free bubble (RFB) [11,24] approaches have been shown to lead to a variation of the multiscale finite element method (MsFEM) [25] (see [35,21] for further details), even though MsFEM is not built by a space enriching procedure. For mixed problems, the method proposed in [3] takes advantage of a splitting of continuous spaces into a direct sum of spaces to build finite dimensional subspaces. The MsFEM [12] can be seen as a particular case of the approach (see [4]) when a zero-order approximation for the flux is used.

The use of element-wise boundary value problems to achieve stability and produce solutions free of oscillations has also emerged as a modern technique to develop discontinuous Galerkin (DG) methods [9,15]. In such a setting, the local boundary conditions are left unknown and selected such that continuity of the solution and a numerical flux across faces is point-wise and weakly assured, respectively. This idea is pursued in [16], but therein, a more involved strategy is adopted to prescribe both the continuity of the pressure and the flux strongly on faces. This results in a discontinuous Petrov–Galerkin (DPG) method containing four fields.

The present work proposes a new family of mixed finite element methods for the Darcy equation specially built to handle heterogenous coefficients. Instead of the standard development of the mixed method, here we start with the elliptic Laplace equation, for which the regularity of the solution is relaxed using element-wise defined Sobolev spaces (as proposed in [9]). Continuity is then weakly imposed through the action of Lagrange multipliers (see [19] for this idea applied within an enriching space strategy). This is known as hybridization and was first proposed in [28,29]. Following these, a family of stable discrete hybrid methods was analyzed in [31]. We take a different approach, wherein we take advantage of an upscaling strategy which is inherent to the problem. More precisely, the exact pressure is shown to be composed of:

- A collection of functions satisfying local Neumann elliptic problems defined in terms of the data and the (unknown) Lagrange multiplier;
- A piecewise constant function that satisfies a global variational formulation of mixed type.

In addition to the weak continuity for the pressure, the approach naturally induces strong continuity of the flux on internal faces since it is represented by the single-valued Lagrange multiplier. Consequently, this methodology provides a post-processed, continuous normal velocity field resulting from the lift of the flux through the element-wise boundary value problems. By taking advantage of the stated infinite-dimensional decomposition, we construct a family of finite element methods with the following properties:

- Stable, with high-order accuracy for the family of elements  $V_0 \times \Lambda_l$ , where  $V_0$  stands for the piecewise constant space for the pressure and  $\Lambda_l$  the polynomial space of order less than or equal to  $l$  for the Lagrange multiplier, defined on faces. Interestingly,  $V_0$  appears as a consequence of the decomposition of the space, so the only approximation space is  $\Lambda_l$ ;
- Include upscaled, element-by-element basis functions which incorporate multiscale or high-contrast features of the flow. This allows the present methods to be precise on very coarse meshes and easily adapted to high-performance parallel computing;
- Produce locally mass conservative velocity fields. This is a suitable feature when it comes to solving multi-phase flows.

By adopting the space  $\Lambda_l$ , some known elements (or version of them) are recovered, namely, the lowest-order RT element when  $l = 0$  (constant on each edge), or the method in [3] when  $l = 1$  (linear). In the case higher-order interpolations are used ( $V_0 \times \Lambda_l$  with  $l > 1$ ), the methods can be related to the ones proposed in [16], although the mathematical framework in which the present methods are derived as well as their final form are intrinsically different. Also, owing to the fact that the primal hybrid methods of [31] are not inf-sup stable for  $V_0 \times \Lambda_l$ , we find that the present methods may be seen as stabilized primal hybrid methods.

In addition to providing the construction of the methods, careful attention is paid to numerical validation, which intends to assess the ability of the methods to handle problems with multiscale and high-contrast coefficients on both structured and unstructured meshes. Also, we verify numerically that the present methods achieve a form of super-convergence in natural norms when the pressure is updated with the solutions of the local problems. For this reason, this paper leaves theoretical proofs of well-posedness and error estimates to be addressed in forthcoming works.

The paper is outlined as follows: the problem statement and the notations used throughout are in Section 2. The weak formulation and the approach to decomposing the solution is then presented in Section 3, which closes with the definition of the finite elements used in the method. The finite element methods, from now on called Multiscale Hybrid-Mixed (MHM)

methods, are introduced and subsequently compared with existing methods in Section 4. Several numerical tests are then presented in Section 5, followed by conclusions in Section 6.

## 2. The model and preliminaries

In what follows, let  $\Omega \subset \mathbb{R}^d$ ,  $d \in \{2, 3\}$ , be an open bounded domain with polygonal boundary  $\partial\Omega := \partial\Omega_D \cup \partial\Omega_N$ , where  $\partial\Omega_D$  and  $\partial\Omega_N$  denote Dirichlet and Neumann boundaries, respectively.

We consider the elliptic problem to find  $p$  such that

$$\mathcal{L}p = f \quad \text{in } \Omega, \quad (1)$$

$$-\mathcal{K}\nabla p \cdot \mathbf{n} = 0 \quad \text{on } \partial\Omega_N, \quad (2)$$

$$p = g_D \quad \text{on } \partial\Omega_D, \quad (3)$$

where  $g_D$  and  $f$  are given regular functions,  $\mathbf{n}$  is the outward normal vector of  $\partial\Omega$ , and

$$\mathcal{L}p := \nabla \cdot (-\mathcal{K}\nabla p). \quad (4)$$

The diffusion coefficient  $\mathcal{K} = \{\mathcal{K}_{ij}\}$  is a symmetric tensor in  $[L^\infty(\Omega)]^{d \times d}$  (with its usual meaning) which is assumed to be uniformly elliptic, i.e., there exist positive constants  $c_1$  and  $c_2$  such that

$$c_1 |\xi|^2 \leq \mathcal{K}_{ij}(\mathbf{x}) \xi_i \xi_j \leq \frac{1}{c_2} |\xi|^2 \quad \forall \xi = \{\xi_i\} \in \mathbb{R}^d, \mathbf{x} \in \bar{\Omega},$$

where  $|\cdot|$  is the Euclidian norm. The diffusion coefficient  $\mathcal{K}$  in (4), also called a permeability coefficient, is free to involve multiscale features and/or high-contrast interfaces in it (see Fig. 1), such as those proposed, respectively, in [25,14] or [17]. If  $\partial\Omega_D = \emptyset$ , then we assume the compatibility condition  $(f, 1)_\Omega = 0$  and  $(p, 1)_\Omega = 0$  hold. Problem (1)–(3) is well-posed in  $H^1(\Omega)$  under these assumptions and additional regularity on  $\mathcal{K}$ , and if functions  $f$  and  $g_D$  are smooth and  $\Omega$  is a convex set, the extra regularity  $p \in H^2(\Omega)$  follows [18, p. 119]. Here, we take the usual definitions for the Sobolev spaces  $H^m(D)$ , where  $m \in \mathbb{Q}$  and  $D$  is an open set, and denote the associated inner product  $(\cdot, \cdot)_{m,D}$ . We write  $L^2(D) := H^0(D)$  and  $(\cdot, \cdot)_D := (\cdot, \cdot)_{0,D}$ . Also, the space  $H(\operatorname{div}, D) := \left\{ \mathbf{v} \in [L^2(D)]^d : \nabla \cdot \mathbf{v} \in L^2(D) \right\}$ .

**Remark 1.** If a non-homogeneous Neumann boundary condition  $-\mathcal{K}\nabla p \cdot \mathbf{n} = g_N$  is prescribed on  $\partial\Omega_N$ , then we assume there exists a function  $p^g$  satisfying such a boundary condition so that the solution decomposes as  $\hat{p} + p^g$ , where  $\hat{p}$  satisfies (1)–(3) with the modified right-hand side  $f - \mathcal{L}p^g$ . Also, in the case of the pure Neumann problem, one requires that the compatibility condition  $(f, 1)_\Omega = (g_N, 1)_{\partial\Omega}$  holds.  $\square$

Our goal in this work is to obtain an accurate approximation of both  $p \in H^1(\Omega)$  and the velocity variable  $\boldsymbol{\sigma}(p) \in H(\operatorname{div}, \Omega)$  given by

$$\boldsymbol{\sigma}(p) := -\mathcal{K}\nabla p. \quad (5)$$

The standard way to deal with the velocity approximation is use (5) in (1)–(3) to yield a problem in mixed form. Also, since a heterogeneous coefficient is involved in the model, it is of particular interest to look for the solution  $p$  and the velocity  $\boldsymbol{\sigma}(p)$  from the perspective of local problems as a way to collect fine-scale contributions in parallel. Such a viewpoint is featured in the works by Hou and Wu [25] and Arbogast [3]. In regard to the present work, we adopt a different perspective: we seek  $p$  as the solution of the elliptic equation in a weaker, broken space which relaxes continuity, allows reconstruction of the velocity, and localizes computations. We detail the approach in the next section, but first we need some definitions and notations.

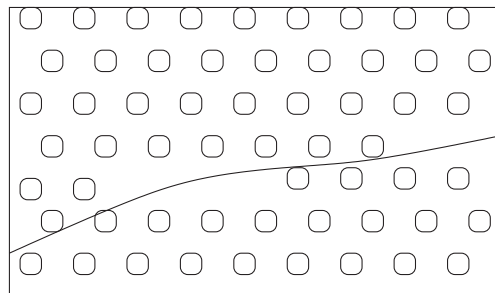


**Fig. 1.** Illustration of a porous domain with an embedded high-contrast interface.

## 2.1. Notation

Let  $\{\mathcal{T}_h\}_{h>0}$  be a family of regular triangulations of  $\Omega$  into elements  $K$ . Each element  $K$  has a boundary  $\partial K$  consisting of faces  $F$ . We define  $h_K := \text{diam}K$ ,  $h_F := \text{diam}F$ , and denote the characteristic length of the partition  $\mathcal{T}_h$  by  $h := \max_{K \in \mathcal{T}_h} h_K$ . Furthermore, denote by  $\mathcal{E}_h$  the set of all faces  $F$  in the triangulation, and decompose this as the set of faces on the boundary  $\mathcal{E}_h^{\partial}$  and as the set of internal faces  $\mathcal{E}_h^0 := \mathcal{E}_h \setminus \mathcal{E}_h^{\partial}$ . We also denote the set of faces *only* on the Neumann (Dirichlet) boundary by  $\mathcal{E}_h^{\partial N}$  (resp.,  $\mathcal{E}_h^{\partial D}$ ) and the set of faces *not* on the Dirichlet (Neumann) boundary by  $\mathcal{E}_h^D := \mathcal{E}_h \setminus \mathcal{E}_h^{\partial D}$  (resp.,  $\mathcal{E}_h^N$ ). To each  $F \in \mathcal{E}_h$  we associate a normal  $\mathbf{n}_F$ , taking care to ensure this is facing outward on  $\partial\Omega$ . We also define  $\mathbf{n}$  to have the property  $\mathbf{n}|_F = \mathbf{n}_F$  on each  $F \in \mathcal{E}_h$ . For each  $K \in \mathcal{T}_h$ , we further denote by  $\mathbf{n}^K$  the outward normal on  $\partial K$ , and let  $\mathbf{n}_F^K := \mathbf{n}^K|_F$  for each  $F \subset \partial K$ .

In addition to the usual Sobolev spaces, we require the notion of broken Sobolev spaces. To this end, we define

$$\begin{aligned} H^m(\mathcal{T}_h) &:= \left\{ v \in L^2(\Omega) : v|_K \in H^m(K), K \in \mathcal{T}_h \right\}, \\ H(\mathbf{div}, \mathcal{T}_h) &:= \left\{ \mathbf{v} \in [L^2(\Omega)]^d : \mathbf{v}|_K \in H(\mathbf{div}, K), K \in \mathcal{T}_h \right\}, \\ H^{\frac{1}{2}}(\mathcal{E}_h) &:= \left\{ \mu \in \prod_{K \in \mathcal{T}_h} H^{\frac{1}{2}}(\partial K) : \exists v \in H^1(\Omega) \text{ s.t. } \mu|_{\partial K} = v|_{\partial K}, K \in \mathcal{T}_h \right\}, \\ H^{-\frac{1}{2}}(\mathcal{E}_h) &:= \left\{ \mu \in \prod_{K \in \mathcal{T}_h} H^{-\frac{1}{2}}(\partial K) : \exists \boldsymbol{\sigma} \in H(\mathbf{div}, \Omega) \text{ s.t. } \mu|_{\partial K} = \boldsymbol{\sigma} \cdot \mathbf{n}|_{\partial K}, K \in \mathcal{T}_h \right\}. \end{aligned}$$

We primarily work with  $V := H^1(\mathcal{T}_h)$  and  $\Lambda := H^{-\frac{1}{2}}(\mathcal{E}_h)$ , and the space

$$\Lambda^N := \left\{ \mu \in \Lambda : \mu|_F = 0, \forall F \in \mathcal{E}_h^{\partial N} \right\}.$$

For these spaces, we require the notion of broken  $L^2$  inner products  $(\cdot, \cdot)_{\mathcal{T}_h}$  and  $(\cdot, \cdot)_{\mathcal{E}_h}$ , which implicitly indicate summation over the respective sets.

Observe that regardless of the value of  $m$ , functions in  $H^m(\mathcal{T}_h)$  generally are multiple-valued on faces  $F \in \mathcal{E}_h^0$ . In order to better understand the behavior of functions in  $V$  on  $\mathcal{E}_h$ , we introduce the notion of jump  $[\![ \cdot ]\!]$  and average value  $\{ \cdot \}$  (see [5]); given a function  $q \in H^1(\mathcal{T}_h)$ , these are defined on face  $F = \partial K_1 \cap \partial K_2 \in \mathcal{E}_h^0$  by

$$[\![ q ]\!]_F := q^{K_1}|_F \mathbf{n}_F^{K_1} + q^{K_2}|_F \mathbf{n}_F^{K_2}, \quad \{ q \}|_F := \frac{1}{2} (q^{K_1}|_F + q^{K_2}|_F), \quad (6)$$

where  $q^{K_i} \in H^1(K_i)$ ,  $i \in \{1, 2\}$ . Furthermore, we define the jump and average values of vector-valued functions  $\boldsymbol{\sigma} \in [H^1(\mathcal{T}_h)]^2$ , respectively, by

$$[\![ \boldsymbol{\sigma} ]\!]_F := \boldsymbol{\sigma}^{K_1}|_F \cdot \mathbf{n}_F^{K_1} + \boldsymbol{\sigma}^{K_2}|_F \cdot \mathbf{n}_F^{K_2}, \quad \{ \boldsymbol{\sigma} \}|_F := \frac{1}{2} (\boldsymbol{\sigma}^{K_1}|_F + \boldsymbol{\sigma}^{K_2}|_F).$$

For faces  $F \subset \partial\Omega$  with incident triangle  $K$ , we define the jump of a scalar function and average value of a vector-valued function by

$$[\![ q ]\!]_F := q|_F^K \mathbf{n}_F^K, \quad \{ \boldsymbol{\sigma} \}|_F := \boldsymbol{\sigma}^K|_F.$$

An important identity holds regarding these values,

$$\sum_{K \in \mathcal{T}_h} (\boldsymbol{\sigma}^K \cdot \mathbf{n}^K, q^K)_{\partial K} = (\{ \boldsymbol{\sigma} \}, [\![ q ]\!]_{\mathcal{E}_h} + (\{ \boldsymbol{\sigma} \}, \{ q \})_{\mathcal{E}_h^0}). \quad (7)$$

If  $\mu = \boldsymbol{\sigma} \cdot \mathbf{n}$  has the property  $\mu \in \Lambda$  (i.e., it is single-valued on cell interfaces), then by (7)

$$\sum_{K \in \mathcal{T}_h} (\mu \mathbf{n} \cdot \mathbf{n}^K, q^K)_{\partial K} = (\mu \mathbf{n}, [\![ q ]\!]_{\mathcal{E}_h}). \quad (8)$$

We note that the inner-product  $(\cdot, \cdot)_{\partial K}$  may be interpreted as a product of duality when  $\mu \in \Lambda$ , and we adopt the right-hand side of (8) as a formal representation of the left-hand side throughout the rest of this paper.

We shall require some finite-dimensional spaces. First, let

$$V_0 := \{q \in V : q|_K \in \mathbb{P}_0(K), \forall K \in \mathcal{T}_h\}. \quad (9)$$

Next, given  $l \in \mathbb{N}$ , we define

$$\Lambda_l := \left\{ \mu_l \in \Lambda^N : \mu_l|_F \in \mathbb{P}_l(F), \forall F \in \mathcal{E}_h \right\}, \quad (10)$$

where  $\mathbb{P}_k(K)$  (respect.  $\mathbb{P}_k(F)$ ) stands for the space of piecewise polynomials of degree less than or equal to  $k$  on  $K$  (respect.  $F$ ). The functions in  $\Lambda_l$  may be discontinuous at the vertices (see Fig. 2). Finally, it is useful to consider the local  $L^2$ -orthogonal projection  $\Pi_K(\cdot)$  onto the constant space, i.e.,  $\Pi_K(q) := \frac{1}{|K|} \int_K q$ .

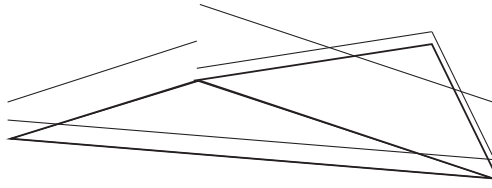


**Fig. 2.** Illustration of a function in  $\Lambda_0$  living only on edges.

### 3. A weak formulation

Our starting point is a formulation of the problem (1)–(3) on the space  $V$  such that continuity on faces is weakly enforced through the action of Lagrange multipliers  $\lambda \in \Lambda^N$ . That is, we will work with the following weak problem: *Find  $(p, \lambda) \in V \times \Lambda^N$  such that*

$$B(p, \lambda; q, \mu) = F(q, \mu), \quad \forall (q, \mu) \in V \times \Lambda^N, \quad (11)$$

where

$$B(p, \lambda; q, \mu) := (\mathcal{K}\nabla p, \nabla q)_{\mathcal{T}_h} + (\lambda \mathbf{n}, [\![q]\!])_{\mathcal{E}_h} + (\mu \mathbf{n}, [\![p]\!])_{\mathcal{E}_h}, \quad (12)$$

$$F(q, \mu) := (f, q)_{\mathcal{T}_h} + (\mu, g_D)_{\mathcal{E}_h^{op}}. \quad (13)$$

This is the standard hybrid formulation from which the primal hybrid methods arise, and is shown to be well-posed with  $p \in H^1(\Omega)$  in [31].

It is interesting to interpret (11) when extra regularity  $(p, \lambda) \in H^2(\mathcal{T}_h) \times H^{\frac{1}{2}}(\mathcal{E}_h)$  holds. First, testing (11) with  $(q, 0) \in V \times \Lambda^N$ , performing integration by parts, and applying the identity (8), it holds

$$\begin{aligned} (f, q)_{\mathcal{T}_h} &= B(p, \lambda; q, 0) \\ &= (\mathcal{K}\nabla p, \nabla q)_{\mathcal{T}_h} + (\lambda \mathbf{n}, [\![q]\!])_{\mathcal{E}_h} \\ &= (\mathcal{L}p, q)_{\mathcal{T}_h} + \sum_{K \in \mathcal{T}_h} (-\boldsymbol{\sigma}(p) \cdot \mathbf{n}^K + \lambda \mathbf{n} \cdot \mathbf{n}^K, q)_{\partial K}. \end{aligned}$$

Standard arguments show the equation above may be written in the following operator form

$$\mathcal{L}p = f \quad \text{in } K, \quad (14)$$

$$\boldsymbol{\sigma}(p) \cdot \mathbf{n} = \lambda \quad \text{on } F \subset \partial K. \quad (15)$$

Next, testing (11) with functions  $(0, \mu) \in V \times \Lambda^N$  introduces the global constraints

$$[\![p]\!] = \mathbf{0} \quad \text{on } F \in \mathcal{E}_h^0, \quad (16)$$

$$p = g_D \quad \text{on } \partial \Omega_D. \quad (17)$$

Additional global constraints on the solution  $p$  may be revealed by (15) and the essential boundary condition satisfied by  $\lambda \in \Lambda^N$ , i.e.,

$$[\![\boldsymbol{\sigma}(p)]\!] = \mathbf{0} \quad \text{on } F \in \mathcal{E}_h^0, \quad (18)$$

$$\boldsymbol{\sigma}(p) \cdot \mathbf{n} = 0 \quad \text{on } \partial \Omega_N. \quad (19)$$

**Remark 2.** It is known that  $p \in H^2(\mathcal{T}_h)$  satisfies (1)–(3) if and only if it satisfies (14)–(19) (see, e.g., [9]). Following the viewpoint used in [9], conditions (16) and (18) are seen as equations to be satisfied either strongly or weakly.  $\square$

At this point, we see that (11) naturally indicates the solution must satisfy local problems (14) and (15). Also, observe that the local problems have a unique solution in  $H^1(K) \cap L_0^2(K)$  since the following local compatibility condition holds (select  $(q, \mu) = (1_K, 0)$  in (11))

$$\int_K f = \int_{\partial K} \lambda \mathbf{n} \cdot \mathbf{n}^K. \quad (20)$$

Therefore, problem (14) and (15) establishes a way to eliminate  $p$ , up to its constant in each  $K \in \mathcal{T}_h$ , in terms of  $\lambda$  and  $f$ . We take advantage of this observation in Section 3.1 to characterize the pressure  $p$  and the velocity  $\boldsymbol{\sigma}(p)$  in  $H^1(\mathcal{T}_h)$  and  $H(\operatorname{div}, \Omega)$ , respectively.

### 3.1. A characterization of the solution

In order to characterize the solution to (11), we begin by decomposing the space  $V$ . Consider the space

$$W := V \cap L_0^2(\mathcal{T}_h)$$

and its orthogonal complement in  $V$ . First, define the  $L^2$ -orthogonal projection operator  $\Pi(\cdot)$  which acts on  $V$  and has image  $V_0$  by the property that for  $q \in V$ ,  $\Pi(q)|_K = \Pi_K(q)$ . It is easy to see that  $W \equiv \ker \Pi = (\mathcal{I} - \Pi)(V)$ , where  $\mathcal{I}$  stands for the identity operator. Therefore, since  $\Pi(V) = V_0$ , it follows that

$$V = V_0 \oplus W. \quad (21)$$

Hence, a function  $q \in V$  admits the following expansion

$$q = \bar{q} + \tilde{q},$$

in terms of unique  $\bar{q} \in V_0$  and  $\tilde{q} := q - \bar{q} \in W$ . Adopting the characterization (21) of  $V$  and performing static condensation, we state (11) in the following equivalent form: *Find  $(p, \lambda) \in V \times \Lambda^N$  such that*

$$B(p, \lambda; q_0, \mu) = F(q_0, \mu), \quad \forall (q_0, \mu) \in V_0 \times \Lambda^N, \quad (22)$$

$$B(p, \lambda; w, 0) = F(w, 0), \quad \forall w \in W, \quad (23)$$

using the definitions (12) and (13) of  $B(\cdot, \cdot)$  and  $F(\cdot)$ , as well as identity (8), we find that (23) is a collection of the following problems on each  $K \in \mathcal{T}_h$ : *Find  $\tilde{p}|_K \in H^1(K) \cap L_0^2(K)$  such that*

$$(\mathcal{K}\nabla\tilde{p}, \nabla w)_K = (f, w)_K - (\lambda \mathbf{n} \cdot \mathbf{n}^K, w)_{\partial K}, \quad \forall w \in H^1(K) \cap L_0^2(K), \quad (24)$$

where we used  $\tilde{p}|_K \in \mathbb{R}$ . We observe that problem (24) allows us to eliminate  $\tilde{p} \in W$  in terms of  $f$  and the solution  $\lambda$ . Furthermore, the linearity of the problem allows us to identify components  $p^\lambda, p^f \in W$  such that

$$\tilde{p} = p^\lambda + p^f,$$

where for each  $K \in \mathcal{T}_h$ ,  $p^\lambda|_K$  and  $p^f|_K$  are the unique functions in  $H^1(K) \cap L_0^2(K)$  satisfying

$$(\mathcal{K}\nabla p^\lambda, \nabla w)_K = -(\lambda \mathbf{n} \cdot \mathbf{n}^K, w)_{\partial K}, \quad \forall w \in H^1(K) \cap L_0^2(K), \quad (25)$$

$$(\mathcal{K}\nabla p^f, \nabla w)_K = (f, w)_K, \quad \forall w \in H^1(K) \cap L_0^2(K). \quad (26)$$

To introduce an operator form of (25) and (26), we first define constant  $C_K^\lambda$  in each  $K \in \mathcal{T}_h$  by

$$(C_K^\lambda, q_0)_K = (\lambda \mathbf{n} \cdot \mathbf{n}^K, q_0)_{\partial K}, \quad \forall q_0 \in \mathbb{P}_0(K) \iff C_K^\lambda = \frac{1}{|K|} \int_{\partial K} \lambda \mathbf{n} \cdot \mathbf{n}^K. \quad (27)$$

Next, since the left-hand side in the equivalence in (27) is the (local) compatibility condition for problem (25), we may now write (25) as

$$\mathcal{L}p^\lambda = C_K^\lambda \quad \text{in } K, \quad (28)$$

$$\boldsymbol{\sigma}(p^\lambda) \cdot \mathbf{n}_F = \lambda \quad \text{on } F \subset \partial K.$$

Following the same procedure, we may also rewrite (26) in an operator form

$$\mathcal{L}p^f = f - \Pi_K(f) \quad \text{in } K, \quad (29)$$

$$\boldsymbol{\sigma}(p^f) \cdot \mathbf{n}_F = 0 \quad \text{on } F \subset \partial K.$$

Hence, functions  $p^\lambda$  and  $p^f$  in the space  $W$  are the unique solutions to (28) and (29) (or equivalently (25) and (26)) in each  $K \in \mathcal{T}_h$ , respectively.

Let us turn to Eq. (22), and interpret it as a global problem for piecing solutions to the local problems (25) and (26) together by selecting the appropriate constant  $\bar{p}$  in each element. To highlight this, we substitute the solutions of local problems (25) and (26) (or equivalently (28) and (29)) into (22) to come up with the following global problem: *Find  $(\bar{p}, \lambda) \in V_0 \times \Lambda^N$  such that*

$$(\mu \mathbf{n}, [\![\bar{p} + p^\lambda]\!])_{\mathcal{E}_h} + (\lambda \mathbf{n}, [\![q_0]\!])_{\mathcal{E}_h} = F(q_0, \mu) - (\mu \mathbf{n}, [\![p^f]\!])_{\mathcal{E}_h}, \quad \forall (q_0, \mu) \in V_0 \times \Lambda^N, \quad (30)$$

where  $p^\lambda$  and  $p^f$  solves (25) and (26), respectively. Therefore, the collection of problems (25) and (26) allows us to define operator-driven subspaces of  $V$  in which the solution

$$p = \bar{p} + p^\lambda + p^f \quad (31)$$

exists. To this end, define  $V_{\Lambda^N} \subset V$  as the subspace of all possible solutions to (25) (for each  $\lambda \in \Lambda^N$ ) and  $V_f \subset V$  as the one-dimensional subspace spanned by the solution of (26). Now, since  $V_{\Lambda^N} \cap V_f = \{0\}$ , the pressure  $p$  given in (31) is such that

$$p \in V_0 \oplus V_{\Lambda^N} \oplus V_f. \quad (32)$$

### 3.1.1. An equivalent formulation

Hidden in the statement of the global problem (30) is a mixed form of the elliptic problem (1). First, consider the term tested against  $q_0$  in (30). Observing that  $\mathcal{L}p^\lambda = \nabla \cdot \boldsymbol{\sigma}(p^\lambda)$ , we use identity (8) and Eqs. (27) and (28) to establish

$$\begin{aligned} (\lambda \mathbf{n}, [\![q_0]\!])_{\mathcal{E}_h} &= \sum_{K \in \mathcal{T}_h} (\lambda \mathbf{n} \cdot \mathbf{n}^K, q_0)_{\partial K} \\ &= (C_K^\lambda, q_0)_{T_h} \\ &= (\nabla \cdot \boldsymbol{\sigma}(p^\lambda), q_0)_{T_h}. \end{aligned} \quad (33)$$

Next, gathering the terms tested against  $\mu$  together, applying identity (8), problem (25) with the fact  $p^\lambda + p^f \in W$ , and the procedure to establish (33), it holds

$$\begin{aligned} (\mu \mathbf{n}, [\![\bar{p} + p^\lambda + p^f]\!])_{\mathcal{E}_h} &= \sum_{K \in \mathcal{T}_h} (\mu \mathbf{n} \cdot \mathbf{n}^K, \bar{p} + p^\lambda + p^f)_{\partial K} \\ &= -(\nabla(p^\lambda + p^f), \mathcal{K}\nabla p^\mu)_{T_h} + (\nabla \cdot \boldsymbol{\sigma}(p^\mu), \bar{p})_{T_h} \\ &= -(\mathcal{K}^{-1}\boldsymbol{\sigma}(p^\lambda), \boldsymbol{\sigma}(p^\mu))_{T_h} - (f, p^\mu)_{T_h} + (\nabla \cdot \boldsymbol{\sigma}(p^\mu), \bar{p})_{T_h}, \end{aligned} \quad (34)$$

where we used the properties of  $\mathcal{K}$  and problem (26).

Finally, we substitute (33) and (34) into the global problem (30) to find it is equivalent to: Find  $(\bar{p}, \lambda) \in V_0 \times \Lambda^N$  such that

$$(\mathcal{K}^{-1}\boldsymbol{\sigma}(p^\lambda), \boldsymbol{\sigma}(p^\mu))_{T_h} - (\nabla \cdot \boldsymbol{\sigma}(p^\mu), \bar{p})_{T_h} - (\nabla \cdot \boldsymbol{\sigma}(p^\lambda), q_0)_{T_h} = -F(q_0, \mu) - (f, p^\mu)_{T_h}, \quad \forall (q_0, \mu) \in V_0 \times \Lambda^N, \quad (35)$$

where we recall that  $p^\lambda$  and  $p^f$  satisfy (25) and (26) (or equivalently (28) and (29)), respectively.

To summarize, we now have a systematic approach of characterizing the solution to problem (11):

- Find solutions  $p^\lambda + p^f \in V_{\Lambda^N} \oplus V_f$  which satisfy (25) and (26) (or equivalently (28) and (29)) locally, up to the value of  $\lambda \in \Lambda^N$ ;
- Determine the values  $(\bar{p}, \lambda) \in V_0 \times \Lambda^N$  using the global problem (30) (or equivalently (35)).

**Remark 3.** Although the global problem (30) (or (35)) involves the space of piecewise constants, no discretization has been introduced up to this point. The fact that this space is involved in this problem is merely an artifact of the kernel of the local problem (14) and (15).  $\square$

**Remark 4.** Local problems (25) and (26) (or (28) and (29)) naturally embed heterogeneous and/or high-contrast features into the construction of the global weak formulation which are not handled by the mesh resolution. Furthermore, the strategy allows the present method to address multiscale aspects of the solution when they still persist inside of each local problem (25) and (26) (or (28) and (29)) for  $p^\lambda$  and  $p^f$ . Indeed, the current framework may be used recursively on the elliptic local problem (25) and (26) (or (28) and (29)), thereby incorporating multiple scales into the method (35). This is of particular interest in dual-porosity problems (see [26]), for instance.  $\square$

**Remark 5.** The key to obtain (34) is choosing (arbitrarily, and without loss of generality) to lift  $\mu$  from  $\partial K$  into  $K$  by using the same problem (25) as we use to lift  $\lambda$ . This choice conveniently yields the method in the form (35), which is completely defined in terms of integrals on elements rather than edge-based terms.  $\square$

Noting that we are still working in infinite-dimensional spaces, we next present finite element spaces for use in approximations.

## 3.2. Finite element spaces

We recall from (31) that the solution  $p$  is decomposed as

$$p = \bar{p} + p^\lambda + p^f,$$

where the components  $\bar{p}$  and  $p^f$  belong to the finite-dimensional subspaces  $V_0$  and  $V_f$ . On the other hand, the component  $p^\lambda$  lives in the infinite-dimensional space  $V_{\Lambda^N}$ , and thus, this last space must be approximated.

We choose to approximate  $V_{\Lambda^N}$  with subspaces which are driven by the choice of polynomial subspaces of  $\Lambda$ . Observing that  $\Lambda_l \subset \Lambda^N$  by definition (10), we introduce the approximating subspace  $V_{\Lambda_l} \subset V_{\Lambda^N}$  which consists of solutions  $p^{\mu_l} \in H^1(K) \cap L_0^2(K)$  such that they satisfy, on each  $K \in \mathcal{T}_h$ ,

$$(\mathcal{K}\nabla p^{\mu_l}, \nabla w)_K = -(\mu_l \mathbf{n} \cdot \mathbf{n}^K, w)_{\partial K}, \quad \forall w \in H^1(K) \cap L_0^2(K), \quad (36)$$

where  $\mu_l \in \Lambda_l$  (compare to problem (25)). Since  $\Lambda_l$  is finite-dimensional, we write elements of  $\Lambda_l$  as a finite linear combination, i.e.,

$$\mu_l = \sum_{i=1}^{\dim \Lambda_l} \beta_i \psi_i^l,$$

where  $\{\psi_i^l\}_{i=1}^{\dim \Lambda_l}$  is the Lagrange basis defined on faces in  $\mathcal{E}_h$  and may be discontinuous at vertices. Owing to the linearity of problem (36), it is easily shown that  $V_{\Lambda_l}$  is a finite element space consisting of the degrees of freedom  $\beta_i$  and basis functions  $\eta_i$  defined such that  $\eta_i|_K = \eta_i^K \in H^1(K) \cap L_0^2(K)$ , where

$$(\mathcal{K}\nabla \eta_i^K, \nabla w)_K = -(\psi_i^l \mathbf{n} \cdot \mathbf{n}^K, w)_{\partial K}, \quad \forall w \in H^1(K) \cap L_0^2(K). \quad (37)$$

As a result, we may express an arbitrary element  $p^{\mu_l} \in V_{\Lambda_l}$  as

$$p^{\mu_l} = \sum_{i=1}^{\dim \Lambda_l} \beta_i \eta_i. \quad (38)$$

We depict in Figs. 3 and 4 examples of basis functions  $\eta_i^K$  in the case  $\mathcal{K} = \mathcal{I}$ .

At this point, we remark that we have fully defined a finite element space

$$V_0 \oplus V_{\Lambda_l} \oplus V_f \subset V, \quad (39)$$

by defining  $V_{\Lambda_l}$  in terms of solutions to (36) and  $V_f$  in terms of (26). On the other hand, we are still presented with the difficulty of solving these problems. In fact, it may be necessary to solve them locally using a two-level finite element method. In summary, two types of approximation might exist in the current approach:

- (i) *global approximation*: a result of defining  $V_{\Lambda_l}$  using  $\Lambda_l$  as outlined previously;
- (ii) *local approximation*: in the case the basis forming  $p^{\mu_l}$  and  $p^f$  are not known exactly, we must use a local numerical method to yield an approximate basis to form  $p_h^{\mu_l} \approx p^{\mu_l}$  and  $p_h^f \approx p^f$ .

Although it is very likely a two-level local discretization will be required, cases do exist for which it is not. For instance, if  $f \in \mathbb{R}$ , then  $p^f = 0$ . Also, in the case that  $l = 0$  and  $\mathcal{K} = \alpha \mathcal{I}$ , where  $\alpha \in \mathbb{R}^+$  on each  $K \in \mathcal{T}_h$ , we find the basis functions  $\eta_F^K$  associated with  $F \subset \partial K$  exhibit the local definition (see [7])

$$\eta_F^K = -\frac{h_F \mathbf{n}_F \cdot \mathbf{n}_F^K}{d|K|\alpha} \left( \frac{|\mathbf{x}|^2}{2} - \mathbf{x} \cdot \mathbf{x}_F + C_F \right), \quad (40)$$

with  $C_F$  being a constant which ensures  $\int_K \eta_F^K = 0$  and  $\mathbf{x}_F$  the vertex of  $K$  opposite face  $F$ .

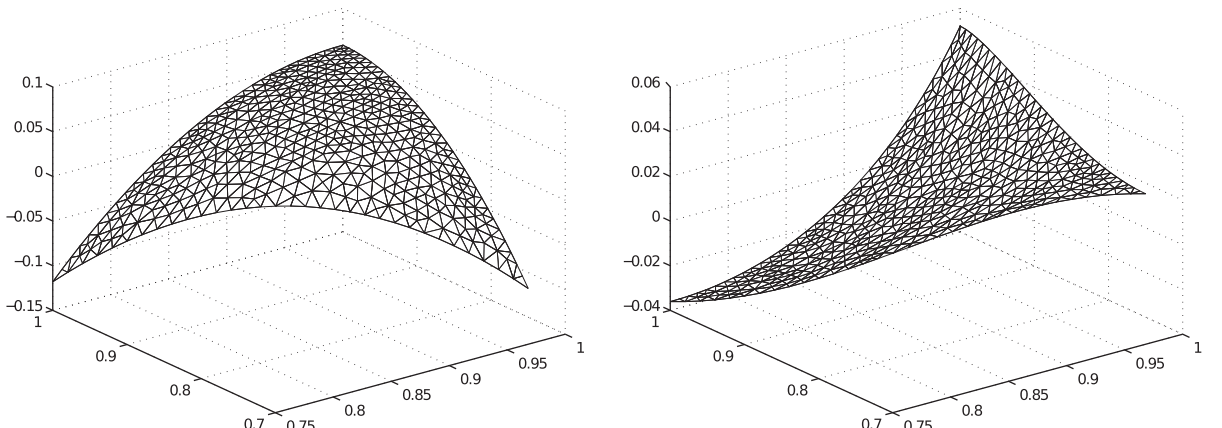


**Fig. 3.** Representative basis functions for  $V_{\Lambda_0}$  (left) and  $V_{\Lambda_1}$  (right).

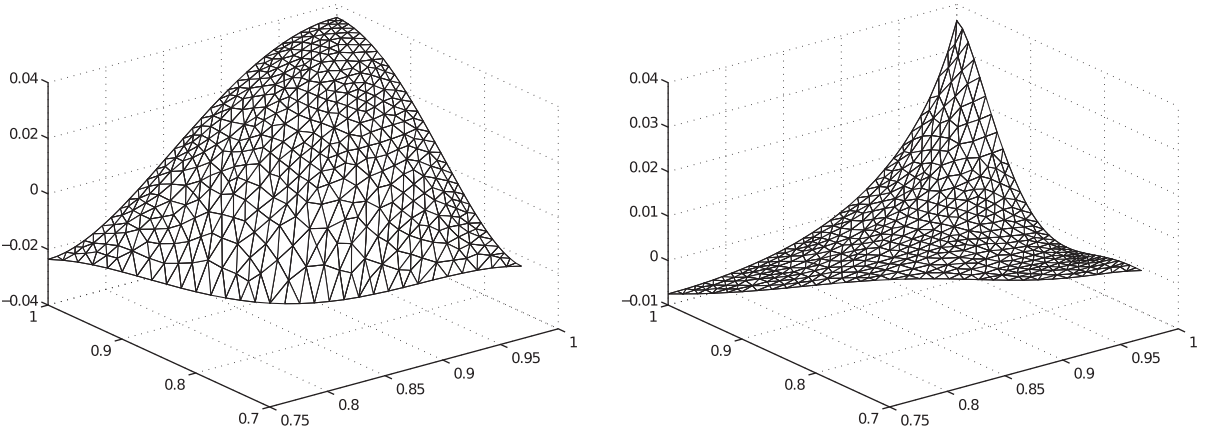


**Fig. 4.** Representative basis functions for  $V_{\Lambda_2}$  (left) and  $V_{\Lambda_3}$  (right).

It is interesting to note that heterogenous and/or high-contrast aspects of the media automatically impact the design of the basis functions as they are driven by the local problems (37) and (26). Also, embedded interfaces are naturally taken care of by local problems (37) and (26), which easily accommodates crossing-edge interfaces thanks to the local boundary conditions. A related approach may be found in [14].

#### 4. The Multiscale Hybrid-Mixed method

Having defined the finite element spaces in the previous section, we now use them to define new finite element methods. Assuming the solutions to (26) and (36) are known exactly, we substitute  $p^{\lambda_l}$  for  $p^\lambda$  in global problem (30) to reveal the MHM method: *Find*  $(p_0, \lambda_l) \in V_0 \times \Lambda_l$  such that, for all  $(q_0, \mu_l) \in V_0 \times \Lambda_l$ , it holds

$$(\mu_l \mathbf{n}, [p_0 + p^{\lambda_l}])_{\mathcal{E}_h} + (\lambda_l \mathbf{n}, [q_0])_{\mathcal{E}_h} = F(q_0, \mu_l) - (\mu_l \mathbf{n}, [p^f])_{\mathcal{E}_h}. \quad (41)$$

We can also substitute  $p^{\lambda_l}$  for  $p^\lambda$  into (35) to yield an equivalent mixed form of the method (41): *Find*  $(p_0, \lambda_l) \in V_0 \times \Lambda_l$  such that,

$$(\mathcal{K}^{-1} \boldsymbol{\sigma}(p^{\lambda_l}), \boldsymbol{\sigma}(p^{\mu_l}))_{\mathcal{T}_h} - (\nabla \cdot \boldsymbol{\sigma}(p^{\mu_l}), p_0)_{\mathcal{T}_h} - (\nabla \cdot \boldsymbol{\sigma}(p^{\lambda_l}), q_0)_{\mathcal{T}_h} = -F(q_0, \mu_l) - (f, p^{\mu_l})_{\mathcal{T}_h}, \quad \forall (q_0, \mu_l) \in V_0 \times \Lambda_l. \quad (42)$$

**Remark 6.** Existence and uniqueness for method (41) (or (42)) holds using standard saddle-point theory (see [10]). It is worth mentioning that the accuracy of  $p_0$  approaching  $\bar{p}$  is dependent on how well  $\lambda_l$  approaches  $\lambda$ . As a consequence, optimal convergence for  $p_0 + p^{\lambda_l} + p^f$  and  $\boldsymbol{\sigma}(p_0 + p^{\lambda_l} + p^f)$  in the natural norms relies only on the capacity of  $\lambda$  to be optimally interpolated by  $\lambda_l$  on faces. These statements are numerically assessed in Section 5 and left to be theoretically proved in [2].  $\square$

**Remark 7.** Note that only a global approximation has been introduced here. The use of a local approximation leads to a two-level methodology, where the functions  $p^{\lambda_l}$  and  $p^f$  in (41) (equivalently (42)) are replaced by their locally approximated discrete counterparts  $p_h^{\lambda_l}$  and  $p_h^f$ . Such computations may be performed either solving the elliptic problems or, if local conformity in  $H(\text{div}, K)$  is needed, solving their mixed counterpart obtained from the recursive procedure mentioned in Remark 4. It is important to note that in either case, method (41) (or (42)) consists of the same number of degrees of freedom, with the local approximation appearing as a preprocessing step which is easily parallelized.  $\square$

**Remark 8.** An easy computation shows that method (41) (or (42)) is locally mass conservative, i.e,

$$\int_K \nabla \cdot \boldsymbol{\sigma}(p^{\lambda_l}) = \int_K f \iff \int_{\partial K} \lambda_l = \int_K f,$$

so that the local conservation feature may be interpreted as the compatibility condition that is fulfilled by the local problems (26) and (36).  $\square$

**Remark 9.** Although we find that the standard mixed formulation of the Laplace problem is a consequence of the approach presented in this paper, we recall that the approach is built on an approximation of  $p$ . Therefore, we may interpret the approach as defining finite elements (i.e., basis functions and degrees of freedom) for which the flux is well-approximated.  $\square$

**Remark 10.** The method may be seen as a divide-and-conquer strategy with a coarse mesh assumed at first level. As such, once basis function are made available, the symmetric indefinite linear system associated to the MHM method has small size. Therefore, standard memory allocation and direct solvers may be adopted with low CPU costs involved. The underlying extra cost arising in pre-computing the basis functions from a two-level (or multi-level if needed) approach turns out to be completely independent and defined element-wise on coarse submeshes as well. In summary, the MHM approach leads to a multi-level algorithm composed of a collection of low cost linear systems which may be solved in parallel using standard tools.  $\square$

#### 4.1. Relationship to existing methods

Among the vast literature concerning stable mixed and hybrid finite element methods for the Laplace and Darcy problems, some are closely related to the one proposed here. Next, we highlight their common features as well as differences, and conclude that the MHM method (41) (or (42)) might be seen as a generalization of previous works (some of them classical). This is, in fact, a direct consequence of the generality of the framework in which the new methods are derived.

##### 4.1.1. A classical mixed method

Assume that  $\partial\Omega \equiv \partial\Omega_N$  and that  $V_{\Lambda_0}$  is used to approximate  $V_{\Lambda^N}$  (i.e., constants are used to approximate the flux on the faces). In the case  $\mathcal{K} = \alpha\mathcal{I}$  with  $\alpha \in \mathbb{R}^+$ , we have the local basis given in (40). Hence, the solution to local problem (36) for  $p^{i_0}|_K$  is

$$p^{i_0}|_K = \sum_{F \subset \partial K} \beta_F \eta_F^K,$$

where  $\beta_F$  stand for the degrees of freedom.

We note that  $-\alpha\nabla\eta_F^K$  is the local basis function associated with the global Raviart–Thomas space. Therefore, the so-called Darcy velocity  $\mathbf{u}^{i_0} := \sigma(p^{i_0})$  is an element of the global  $\text{RT}_0$  space in 2D [30] or  $\text{RTN}_0$  space in 3D [27]. Also, the finite-dimensional problem (42) may be expressed as: *Find*  $(p_0, \lambda_0) \in V_0 \times \Lambda_0$  *such that*

$$\begin{aligned} (\alpha^{-1}\mathbf{u}^{i_0}, \mathbf{u}^{\mu_0})_{T_h} - (\nabla \cdot \mathbf{u}^{\mu_0}, p_0)_{T_h} &= -(f, p^{\mu_0})_{T_h}, \quad \forall \mu_0 \in \Lambda_0, \\ -(\nabla \cdot \mathbf{u}^{i_0}, q_0)_{T_h} &= -(f, q_0)_{T_h}, \quad \forall q_0 \in V_0. \end{aligned}$$

If the term  $(f, p^{\mu_0})_{T_h}$  is neglected (for example, if  $f \in \mathbb{R}$  then it vanishes since  $p^{\mu_0}|_K \in L_0^2(K)$ ), the result is the classical lowest-order Raviart–Thomas method for the mixed form of the elliptic problem (1) (see [10, p. 116], for further details).

**Remark 11.** It is interesting to note the current approach produces an analytically-defined solution  $p^{i_0}$  which may be seen as a local update to the piecewise constant portion of the solution  $p_0$ . Thereby, we can expect superior convergence properties when  $p_0 + p^{i_0}$  is used, up to the regularity assumption on  $p$ . This is assessed in the numerical tests of Section 5. A related super-convergence result has also been pointed out in [4].  $\square$

##### 4.1.2. Multiscale methods

In the case a porous medium involves a more complex permeability coefficient  $\mathcal{K}$ , either due to multiscale or high-contrast aspects for instance, a two-level method must be employed to find an approximate local solution  $p_h^{i_0}$  and  $p_h^f$  of (36) and (26), respectively, that properly handles local fluctuations.

In this context, the present method might be seen as a generalization of some already-known approaches. Indeed, the case when  $\mathcal{K}$  highly oscillates inside  $K \in \mathcal{T}_h$  has been handled in [12] using the local problem (36) assuming  $\Lambda_0$  to discretize flux on faces. However, the second local problem (26) has not been considered, meaning the multiscale method in [12] does not include the term  $(f, p^{\mu_0})_{T_h}$ .

Also, a subgrid upscaling method was introduced in [4] which recovered the method in [12] inside an enhanced space framework. As a result, the method includes the term  $(f, p^{\mu_0})_{T_h}$ , and after some algebraic manipulations, may be seen as the present method using the space  $\Lambda_1$  to approach the flux across faces. Nevertheless, the way the method is built is fundamentally different than the present work, thereby preventing the use of higher-order interpolation spaces  $\Lambda_l, l \geq 2$ . Finally and unlike the present approach, the cited works start with the mixed Darcy problem. As a consequence, the local problems are also of mixed form, and so, a two-level stable finite element pair of spaces is necessarily adopted.

##### 4.1.3. Primal hybrid methods

As mentioned, the primal hybrid methods presented in [31] are a consequence of the same formulation (11) which originates the MHM methods. The difference resides in the fact that the hybrid methods directly assume discrete spaces to approximate  $V$  and  $\Lambda$  rather than decomposing  $V$  using an upscaling strategy.

For sake of clarity, let us recall the methods in [31]. Given the finite element spaces

$$V_k := \{q \in V : q|_K \in \mathbb{P}_k(K), \forall K \in \mathcal{T}_h\},$$

the methods are: *Find*  $(p_k, \lambda_l) \in V_k \times \Lambda_l$  such that

$$B(p_k, \lambda_l; q_k, \mu_l) = (f, q_k)_{\mathcal{T}_h}, \quad \forall (q_k, \mu_l) \in V_k \times \Lambda_l. \quad (43)$$

It is well-known (see [31]) these methods are well-posed if and only if we assume  $k \geq l+1$  when  $l$  is even, or  $k \geq l+2$  when  $l$  is odd.

As a consequence, we observe that the hybrid method (43) with  $k=0$  is not inf-sup stable for any  $l \in \mathbb{N}$ . This method reads: *Find*  $(p_0, \lambda_l) \in V_0 \times \Lambda_l$  such that

$$(\mu_l \mathbf{n}, [\![p_0]\!])_{\mathcal{E}_h} + (\lambda_l \mathbf{n}, [\![q_0]\!])_{\mathcal{E}_h} = (f, q_0)_{\mathcal{T}_h}, \quad \forall (q_0, \mu_l) \in V_0 \times \Lambda_l. \quad (44)$$

Comparing (44) with the MHM methods (41) (or (42)), we observe the presence of an extra term

$$(\mu_l \mathbf{n}, [\![p^{\lambda_l}]\!])_{\mathcal{E}_h}.$$

Interestingly, this additional term is coercive on the following nontrivial subspace

$$\{\mu_l \in \Lambda_l : (\mu_l \mathbf{n}, [\![q_0]\!])_{\mathcal{E}_h} = 0, \forall q_0 \in V_0\},$$

thereby providing a way to “circumvent” the inf-sup condition associated with the primal hybrid methods. From such a perspective, we may interpret the MHM methods as stabilized primal hybrid methods as well.

## 5. Numerical results

We now consider the performance of the MHM method (41). We first verify its convergence properties and then move on to challenging problems involving multiple scales. We note that when the local problems are solved approximately, any number of solvers may be employed. In this work, we consider the effectiveness of the MHM method assuming elliptic local solvers for the local problems (25) and (26) employing  $\mathbb{P}_k$  continuous elements.

### 5.1. An analytical solution

The method is tested for the case  $\mathcal{K} = \mathcal{I}$ , with different choices of  $l$  when approximating  $\lambda$  by  $\lambda_l$ . To shorten the notation, we have adopted the convention  $p_h := p_0 + p^{\lambda_l} + p'$ . All tests are performed on the unit square, using a sequence of structured meshes assuming the exact solution  $p(x, y) = \cos(2\pi x) \cos(2\pi y)$ . This problem has the property that  $f \neq 0$  and satisfies homogeneous Neumann boundary conditions. The errors are measured in the standard  $L^2$  norm  $\|\cdot\|_\Omega^2 = (\cdot, \cdot)_\Omega$ .

Recalling that in the case  $l=0$  the method is the classical lowest-order Raviart–Thomas method with a modified right-hand side, we see the expected classical convergence results presented in the left-hand graph of Fig. 5. Furthermore, we verify in the right-hand graph of Fig. 5 that  $p_h$  converges at order  $\mathcal{O}(h^2)$ , as does  $p_0$  to  $\Pi(p)$ . Such a super-convergence property is inherent in the MHM methods.

Next, in Figs. 6–8 the results consistently show that the choice of interpolation of  $\lambda$  by  $\lambda_l$  drives the convergence rate of the variables involving  $p^{\lambda_l}$ . In fact, we note that  $p_h$  converges at order  $\mathcal{O}(h^{l+2})$ , and that  $\sigma(p_h)$  converges at order  $\mathcal{O}(h^{l+1})$ . In fact,

MHM FINITE ELEMENT METHODS FOR THE DARCY EQUATION

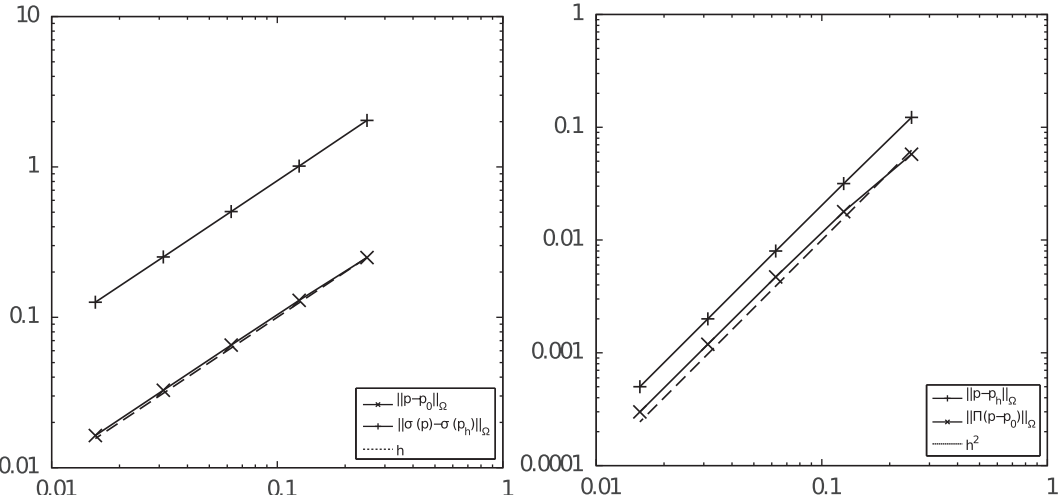
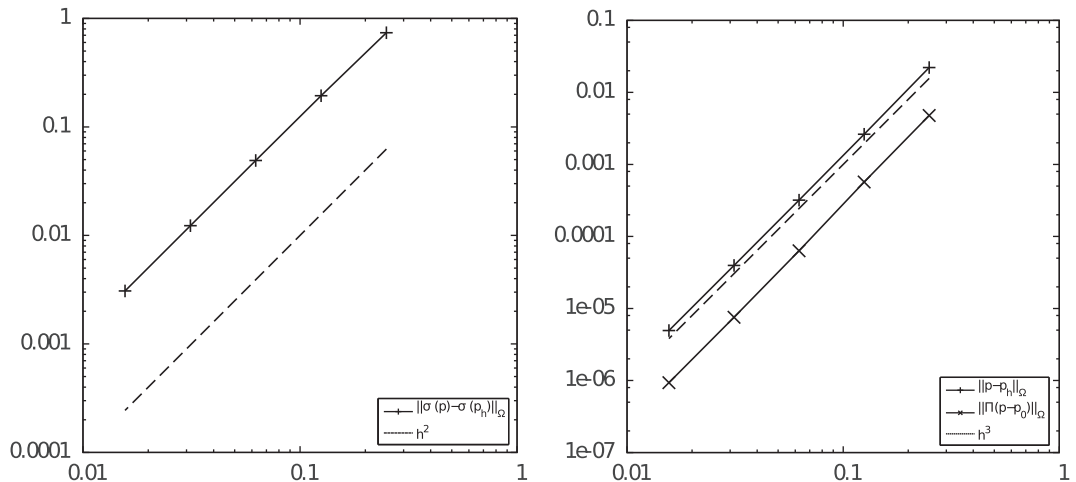
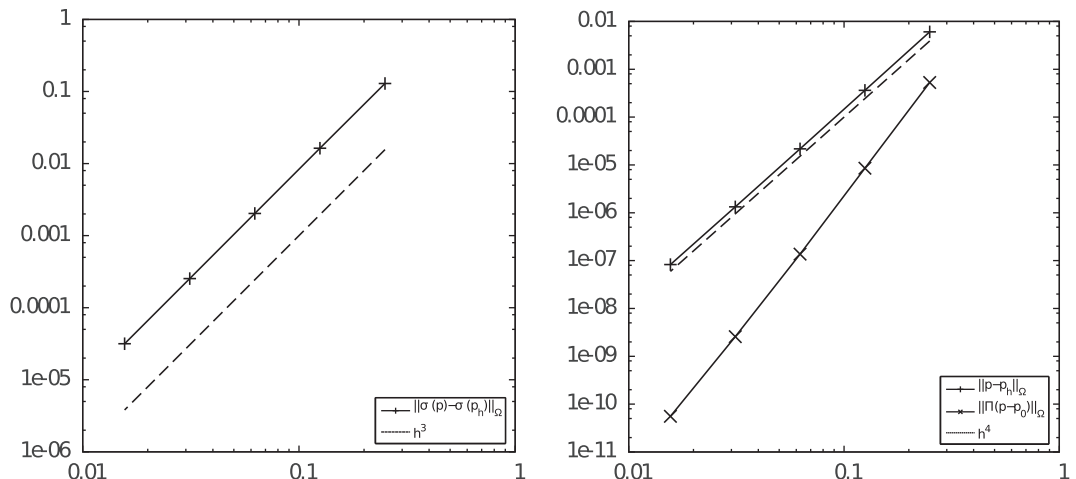
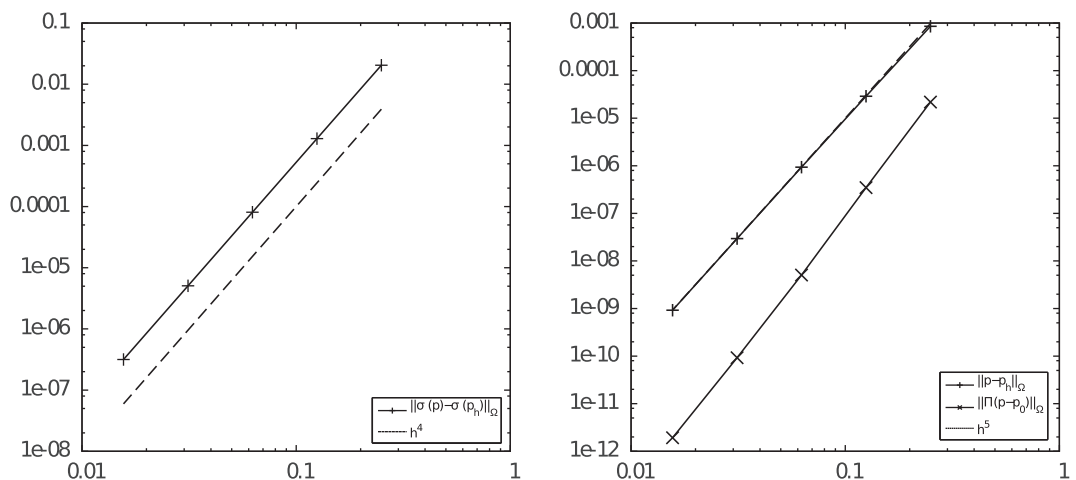


Fig. 5. Error curves for the case  $l=0$ .

Fig. 6. Error curves for the case  $l = 1$ .Fig. 7. Error curves for the case  $l = 2$ .Fig. 8. Error curves for the case  $l = 3$ .

this is not surprising since  $l$  is the only choice of interpolation made in defining the method. As expected,  $p_0$  always converges to  $p$  at order  $\mathcal{O}(h)$ , and so we do not show graphs of this result for  $l \geq 1$ .

We note that all computations at the second level are performed on a one element submesh using polynomial interpolation of degree  $l+1$  in the Laplace problem. This is the minimal interpolation required in this preprocessing step to satisfy optimal convergence. Thereby, it is also interesting to address convergence curves with respect to the total number of degrees of freedom (including the ones arising from submeshes). This is depicted in Fig. 9 (here  $l=2$ ) wherein we observe the convergence of pressure  $p_h$  and velocity  $\sigma(p_h)$  as  $\mathcal{O}\left(\frac{1}{N^{l+2}}\right)$  and  $\mathcal{O}\left(\frac{1}{N^{l+1}}\right)$ , respectively. Here  $N$  is the square root of the total number of degrees of freedom. We further emphasize that, despite the fact that the degrees of freedom necessary to calculate second-level solution as a preprocessing step are included, such an extra computational effort stays reasonable even when the local problems are solved sequentially.

## 5.2. The five-spot problem

Next, we perform tests using the quarter five-spot problem carried out on the unit square with an extraction and an injection well located at the corners (see Fig. 10). We test using both constant and high-contrast permeabilities, as indicated in Fig. 10.

### 5.2.1. The constant permeability case

Figs. 11–14 show results for  $l \in \{0, 2\}$ . First, Fig. 11 shows elevation plots of  $p_h$  in which we can see very similar results for both values of  $l$ . Note the effect of increasing  $l$  clearly allows the solution to be better approached near the wells. In Fig. 12, isolines of the absolute value of  $\sigma(p_h)$  are presented, again with an increase in  $l$  yielding more accurate results. For the case  $l=0$  we used an averaging at vertices to render the plot.

The performance of the method on an unstructured mesh is presented in Figs. 13 and 14. We see results which are very similar to those obtained with a structured mesh.

### 5.2.2. The high-contrast permeability case

Here we show the performance of the method on the quarter five-spot problem with high-contrast permeability (see Fig. 10). Using a structured mesh with 32 triangles along each side of the domain, we have studied this problem using two possible locations for the jump in permeability. The first case assumes the jump in the values of the permeabilities occurs along the edges at  $y=0.5$ . In the second case, the interface is located half-way between edges of the mesh at  $y=0.484375$ . We depict in Fig. 15 a sample local basis functions calculated in the latter case. We can see that the basis functions naturally adapt themselves to incorporate such a jump in the coefficient.

First, Figs. 16–18 show the performance of the method with  $l \in \{1, 3\}$  in the case the jump in the values of the permeabilities occurs at  $y=0.5$ . We observe the capacity of the MHM method in resolving both the solution  $p_h$  and the flux  $\sigma(p_h)$  accurately, with the discontinuity perfectly captured. Improvement in performance is observed for increased  $l$ .

In Fig. 19, we present results when  $l=0$  for the case the interface of jumping permeability is at  $y=0.484375$ . This location places the line of jumping permeabilities along edges of the submesh (a very coarse, structured submesh with two triangles lying along each edge) used to solve each local problem. The local problems are solved using two different strategies. The first one employs a continuous, piecewise quadratic space to solve (36), whereas the second employs the lowest-order

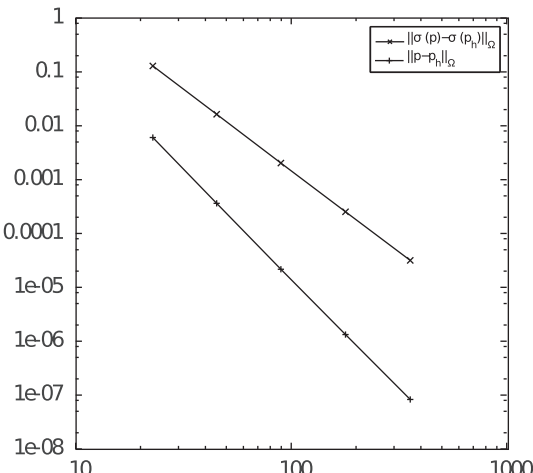
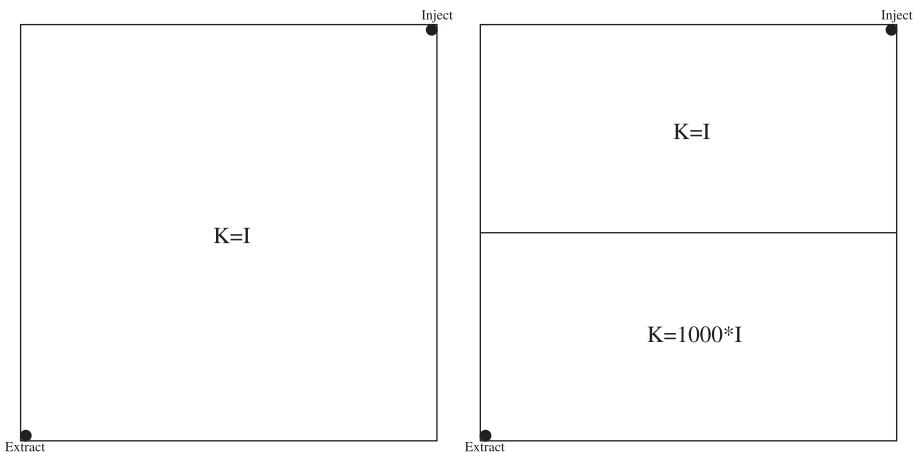
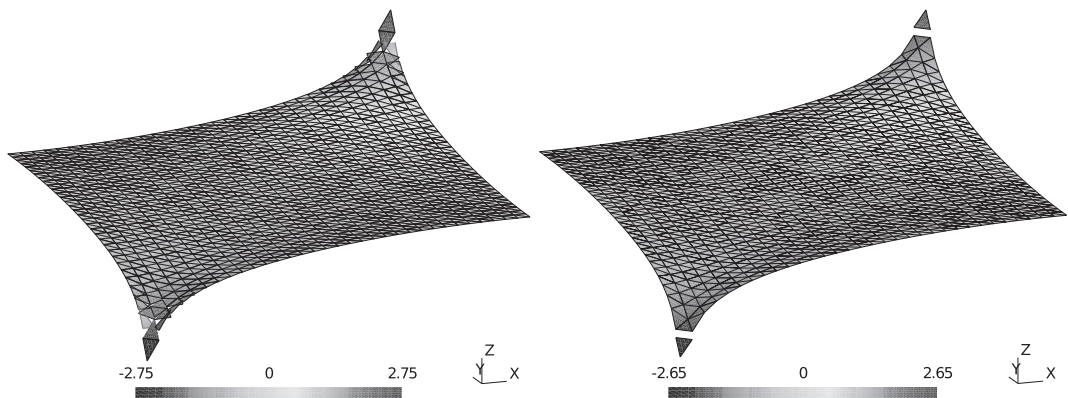


Fig. 9. Error curves relative to  $N$ . Here  $l=2$ .



**Fig. 10.** Description of the quarter five-spot problem, with constant permeability (left) and high-contrast permeability (right).



**Fig. 11.** Elevation plots of  $p_h$  for the quarter five-spot problem using  $l = 0$  (left) and  $l = 2$  (right).

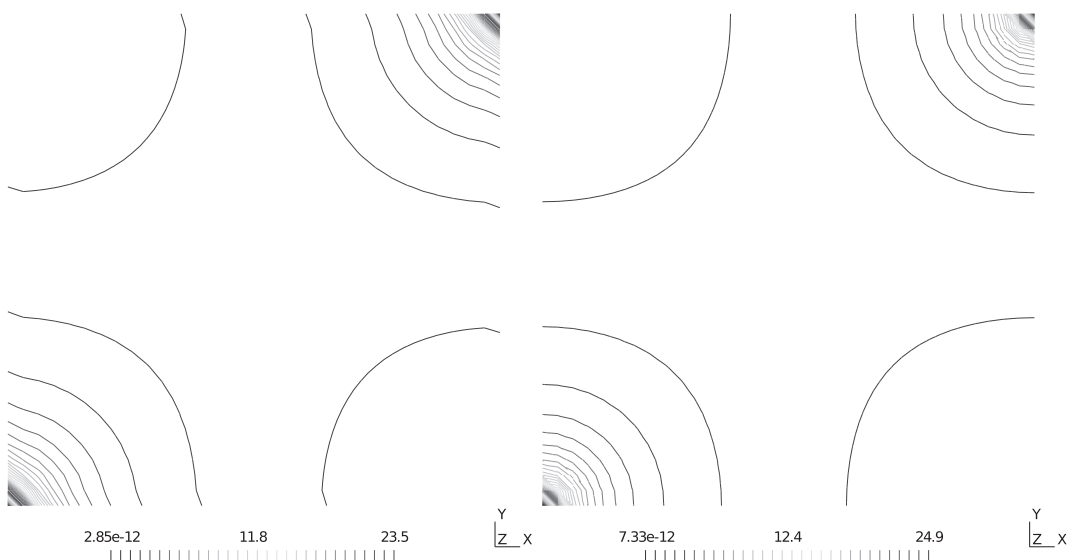


**Fig. 12.** Isolines of the absolute value of  $\sigma(p_h)$  for the quarter five-spot problem using  $l = 0$  (left) and  $l = 2$  (right).

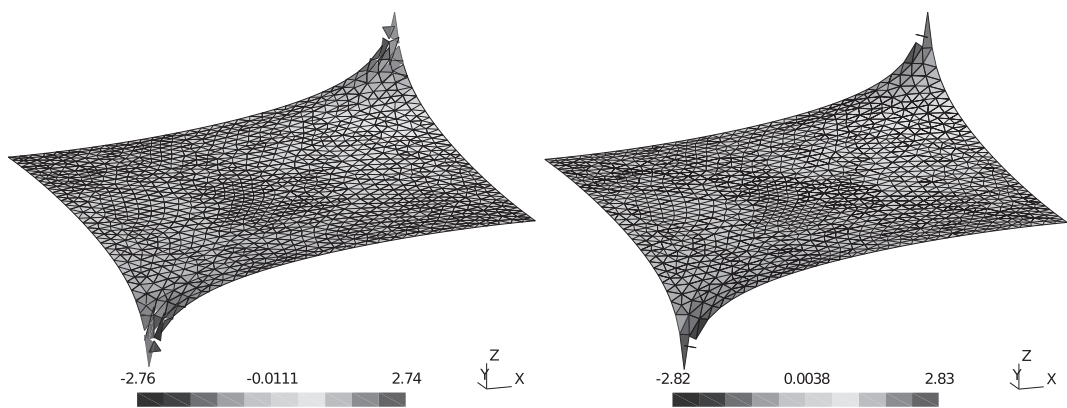


**Fig. 13.** Elevation plots of  $p_h$  for the quarter five-spot problem on an unstructured mesh using  $l = 0$  (left) and  $l = 2$  (right).

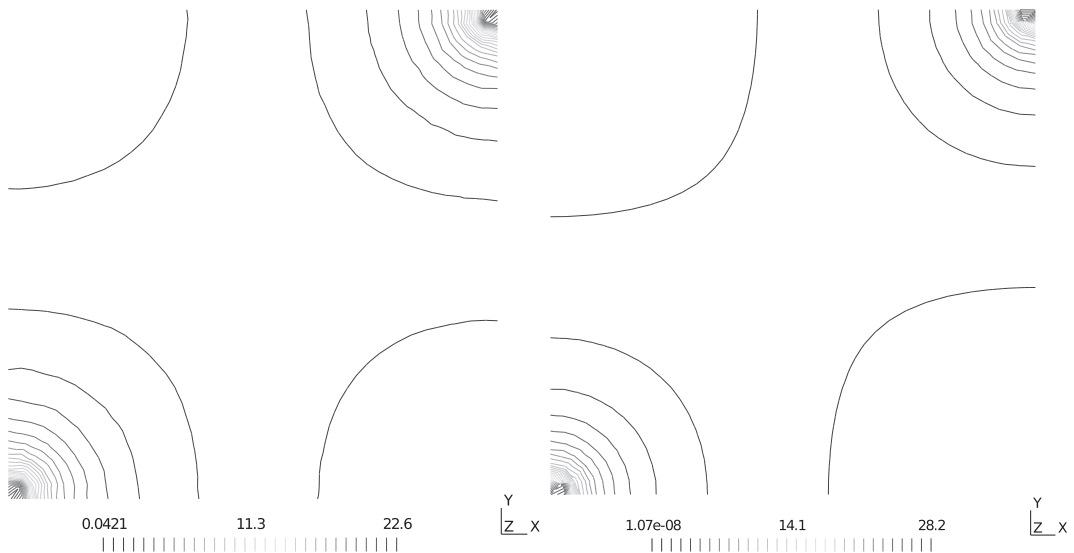


**Fig. 14.** Isolines of the absolute value of  $\sigma(p_h)$  for the quarter five-spot problem on an unstructured mesh using  $l = 0$  (left) and  $l = 2$  (right).

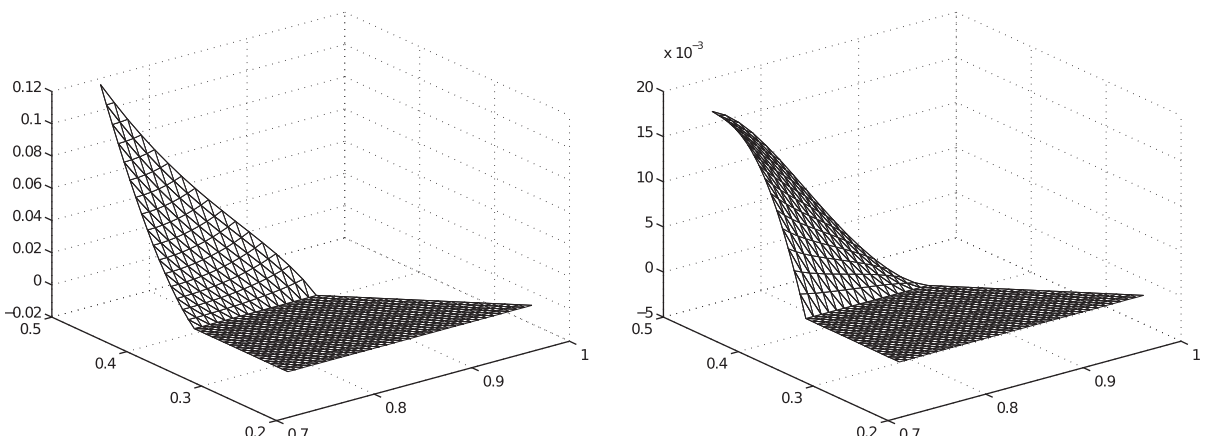


**Fig. 15.** Sample local basis function with a jump in permeability occurring inside. Here  $l = 0$  (left) and  $l = 2$  (right).

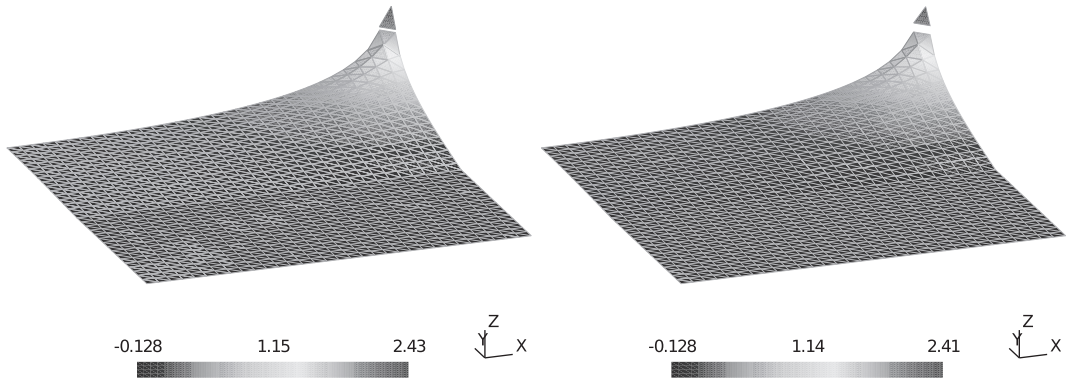


**Fig. 16.** Elevation plots of  $p_h$  for the problem with layered permeability using  $l = 1$  (left) and  $l = 3$  (right).

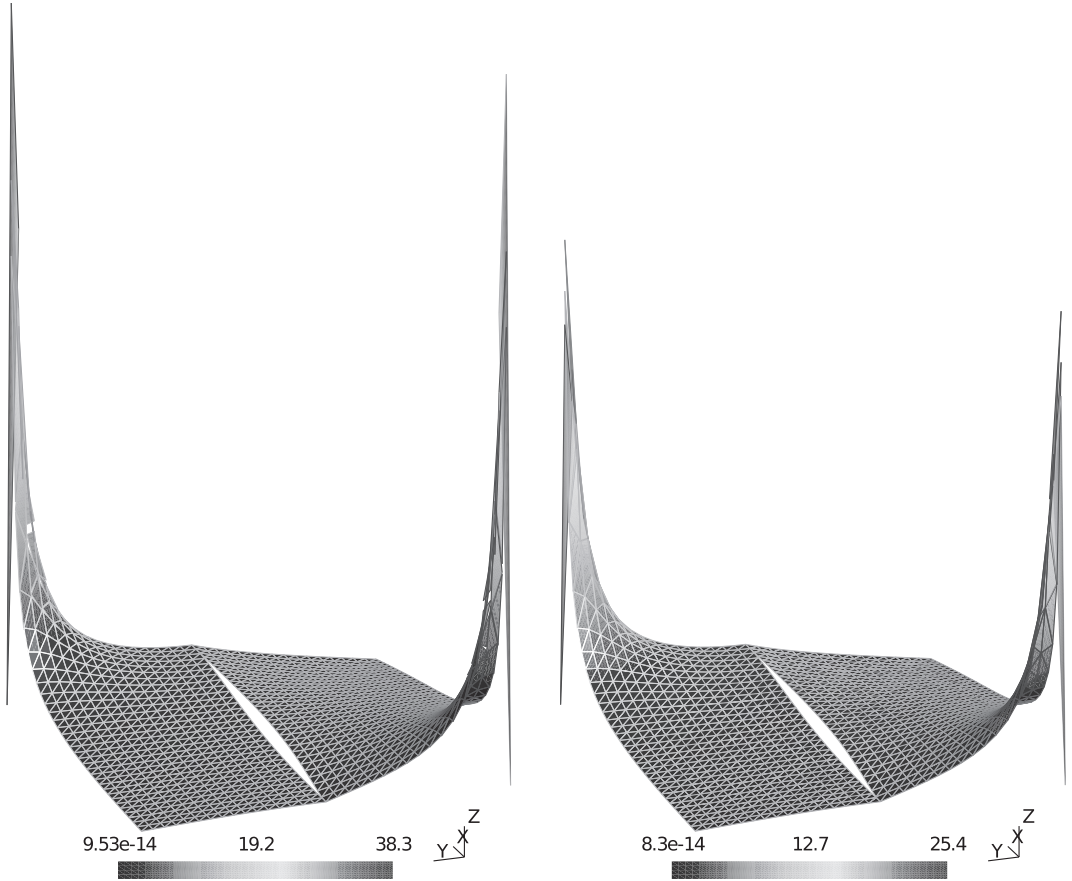


**Fig. 17.** Elevation plots of the absolute value of  $\sigma(p_h)$  for the problem with layered permeability using  $l = 1$  (left) and  $l = 3$  (right).

Raviart–Thomas element to solve a mixed version of (36) as proposed in Remarks 4 and 7. We see that the elevation plots of the absolute value of velocity using these strategies are similar. Localized spurious oscillations of small amplitude occur in the solution near the interface when elliptic local problems are adopted. The use of RT element in the second level keeps the approach conforming in  $H(\operatorname{div}, \Omega)$ , and thereby, corrects such drawbacks.

### 5.3. The oscillatory permeability case

We are interested in the performance of the new methods on a problem with highly-oscillatory coefficients of periodicity  $\varepsilon$  in this section. This problem is defined on the unit square with homogeneous Neumann boundary conditions, right-hand side given by  $f(\mathbf{x}) = 2\pi^2 \cos 2\pi x \cos 2\pi y$ , and permeability coefficient given by

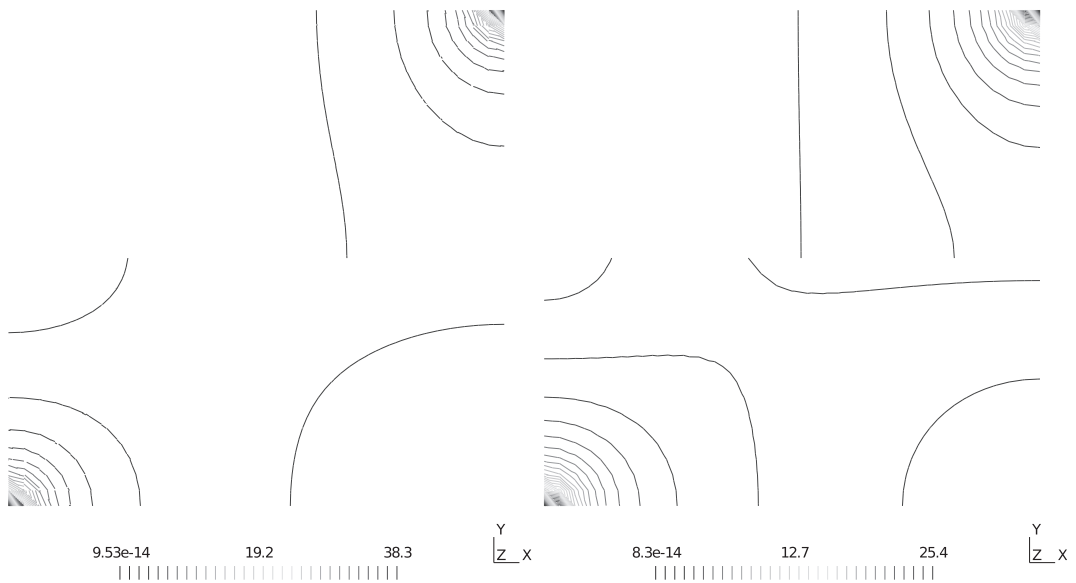


**Fig. 18.** Isolines of the absolute value of  $\sigma(p_h)$  for the problem with layered permeability using  $l = 1$  (left) and  $l = 3$  (right).

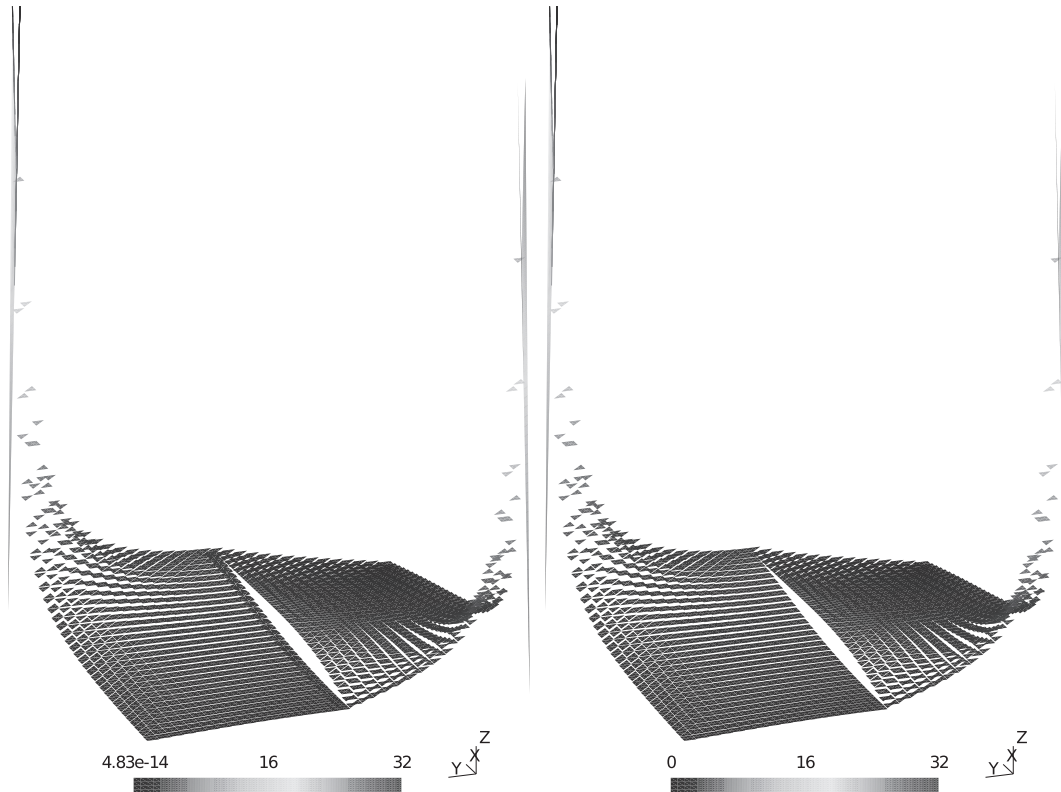


**Fig. 19.** Elevation plots of the absolute value of  $\sigma(p_h)$  using  $l = 0$ . Local problem (36) are solved directly (left) or using a mixed method (right).

$$\mathcal{K}(\mathbf{x}) = \frac{2 + 1.8 \sin \frac{2\pi x}{\varepsilon}}{2 + 1.8 \sin \frac{2\pi y}{\varepsilon}} + \frac{2 + 1.8 \sin \frac{2\pi y}{\varepsilon}}{2 + 1.8 \cos \frac{2\pi x}{\varepsilon}},$$

where here we set  $\varepsilon = \frac{1}{16}$ .

The present method is implemented using both  $l = 0$  and  $l = 2$  on the same coarse mesh. A two-level approach is required, and the mesh inside each element is an unstructured mesh with 32 elements along each side. We depict sample basis functions in the case  $l = 3$  in Fig. 20, wherein we can see the influence of small scales in their design. To provide a basis for comparison, we obtain a solution to problem (1)–(3) using the Galerkin finite element method with linear elements on a very fine mesh of 512 elements in each direction, and we name it the “exact solution.” Next, we solve the problem using the lowest-order Raviart–Thomas element on a coarse mesh of 16 elements in each axis direction.

First, we focus on comparing the piecewise constant solution from the lowest-order Raviart–Thomas method with the exact solution. As shown in Fig. 21, the solution with the lowest-order Raviart–Thomas method captures the large-scale shape correctly, but the amplitude of the solution is significantly incorrect (observe that the solutions are scaled differently). On the other hand, the results in Fig. 22 show both that the MHM methods outperform the lowest-order Raviart–Thomas method, and also that higher-order interpolation of  $\lambda$  makes a significant difference.

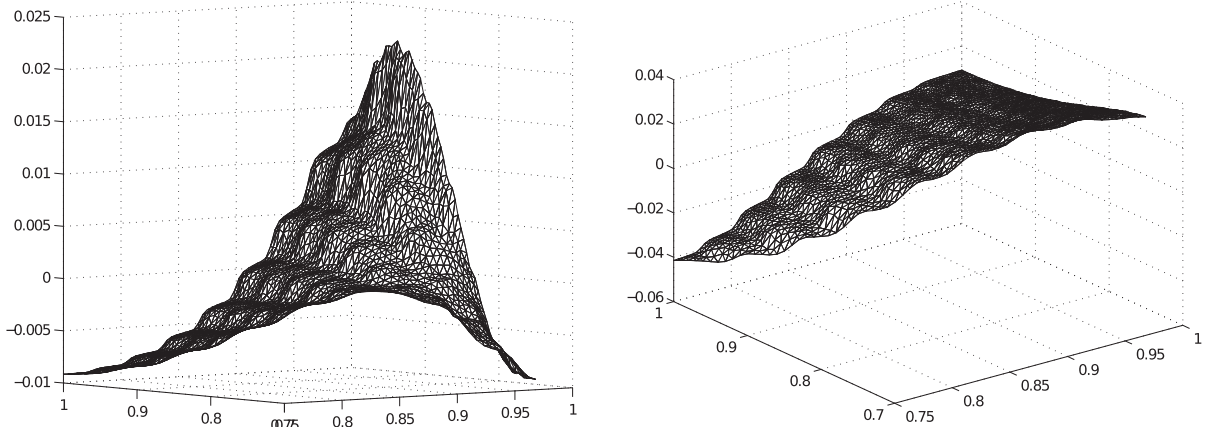


**Fig. 20.** Representative basis functions on a triangle for  $V_{\Lambda_3}$  for oscillatory coefficient cases.

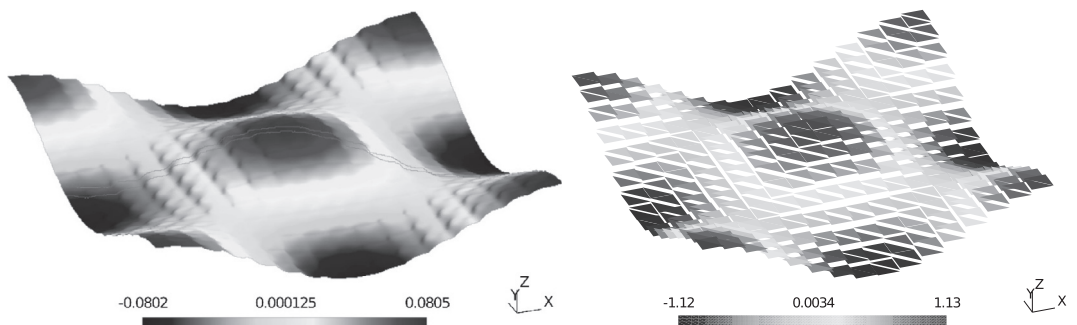


**Fig. 21.** The “exact” pressure (left) and the pressure  $p_0$  computed from the lowest-order Raviart–Thomas element on the coarse mesh (right).

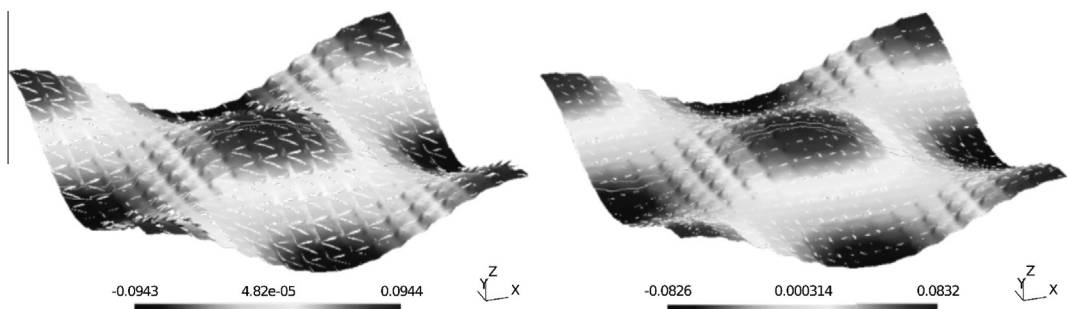


**Fig. 22.** Solutions  $p_0 + p^{2l}$  with  $l = 0$  (left) and  $l = 2$  (right).

To make these assertions even clearer, Figs. 23 and 24 show the piecewise constant solution with the “exact” solution in a vertical cut plane oriented from the lower left-hand corner of the domain to the upper right-hand corner. Fig. 23 shows that the MHM method using  $V_{\Delta_0}$  to approximate  $V_\Lambda$  presents a dramatic improvement over the piecewise constant solution from the lowest-order Raviart–Thomas method, which is completely unacceptable. The results in Figs. 24 and 25 lend support to the assertion that higher-order interpolation makes a significant difference. In Fig. 24, we see the piecewise constant solution from the method using  $l = 2$  is a better approximation than that from the method using  $l = 0$ . Even more interesting, the pressure  $p_0 + p^{\lambda_l}$  provides a very accurate approximation for a larger value of  $l$ , as shown in Fig. 25.

#### 5.4. The multiscale permeability case

As a final validation, we consider the performance of the MHM methods in dealing with a multiscale log-normal permeability field, which is shown in Fig. 27. To determine the field, the unit square has been divided into  $100 \times 100$  squares, and then permeabilities are given by

$$\mathcal{K}(\mathbf{x}) = \alpha e^{\gamma Y(\mathbf{x})},$$

with  $Y$  being a normal random variable and  $\alpha$  and  $\gamma$  taken equal to 1. The value of  $Y$  is taken to be constant on each of the squares, leading to constant permeabilities on each of them. Also, a homogeneous right hand side is taken, with Neumann

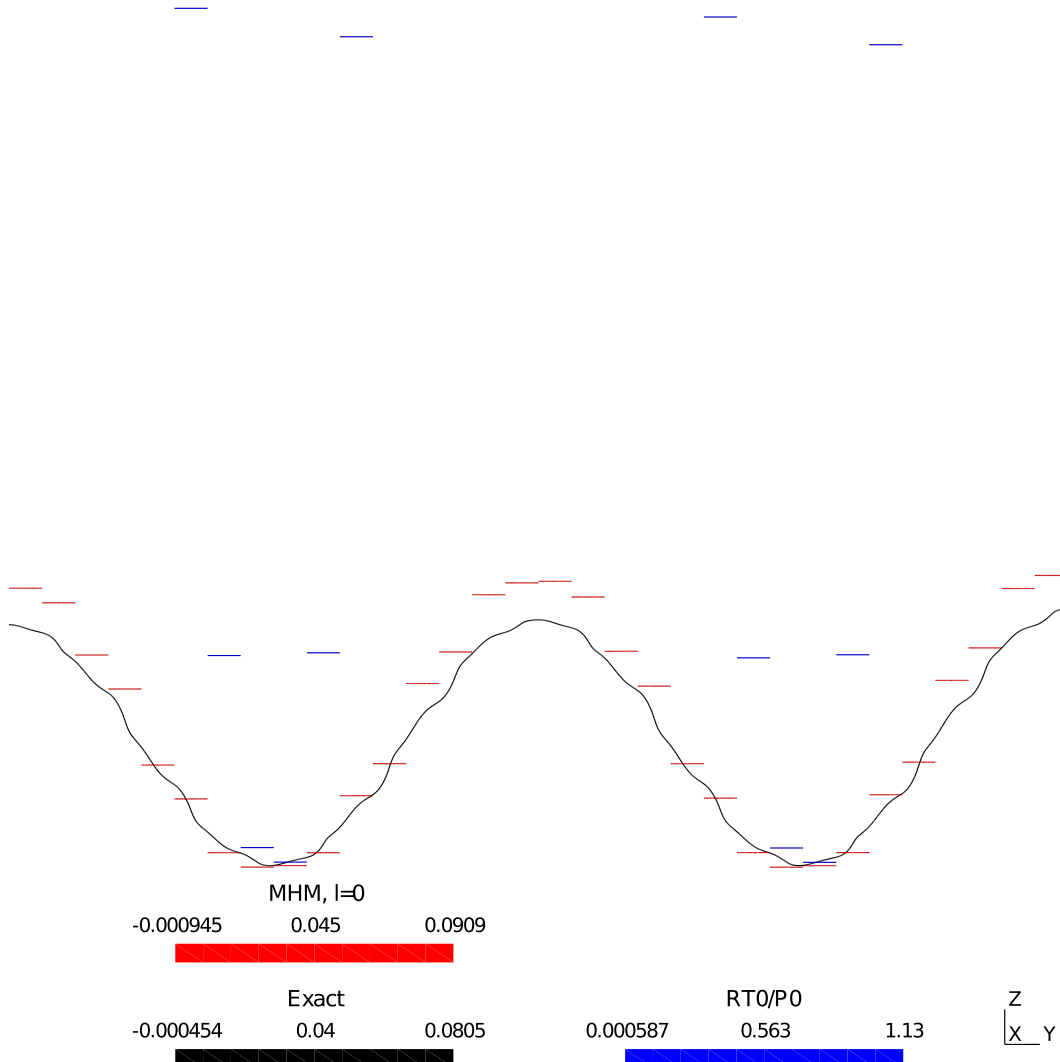


**Fig. 23.** Profiles of the constant pressure solution  $p_0$ . We show the solution from the lowest-order Raviart–Thomas method (blue) and the MHM method with  $l = 0$  (red) together with the “exact” solution (black). (For interpretation of the references to color in this figure legend, the reader is referred to the web version of this article.)

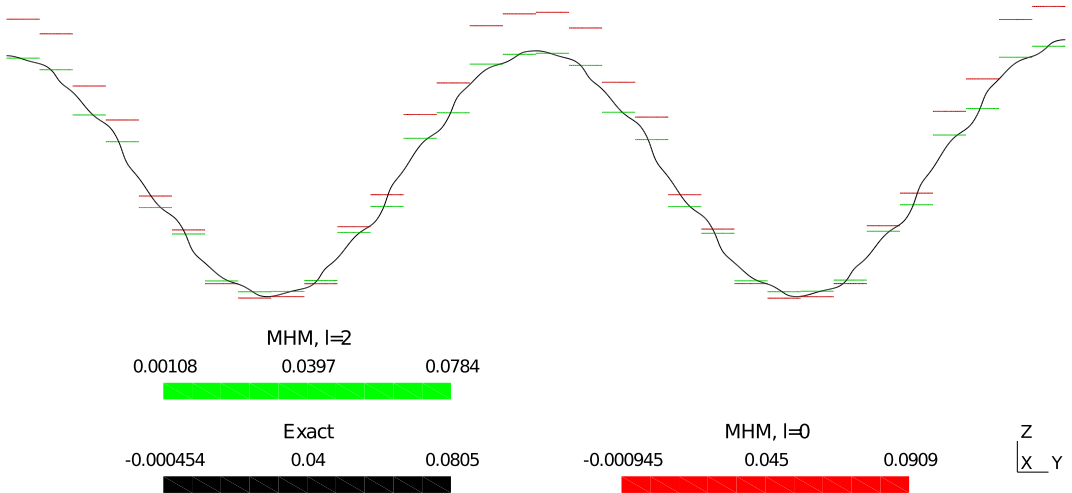


**Fig. 24.** Profiles of solutions  $p_0$  from the MHM methods using both  $l = 0$  (red) and  $l = 2$  (green) are shown in relation to the “exact” solution (black). (For interpretation of the references to color in this figure legend, the reader is referred to the web version of this article.)

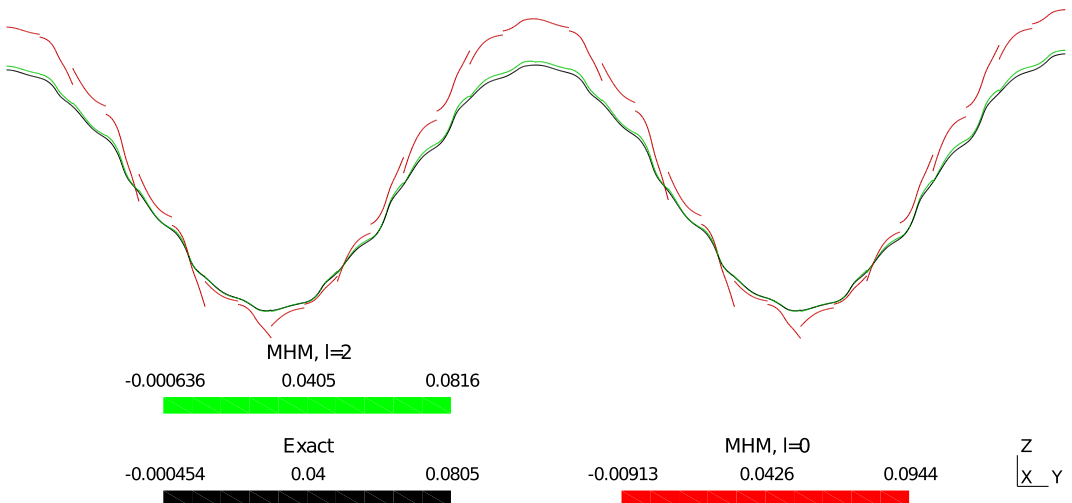


**Fig. 25.** Profiles of  $p_0 + p^{(i)}$  from the MHM methods using both  $l = 0$  (red) and  $l = 2$  (green) are shown in relation to the “exact” solution (in black). (For interpretation of the references to color in this figure legend, the reader is referred to the web version of this article.)

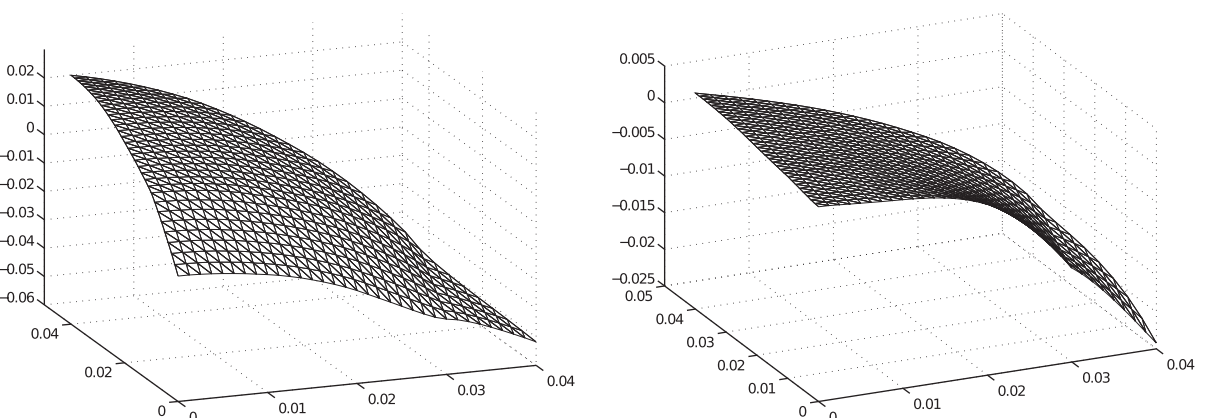


**Fig. 26.** Sample local basis functions with multiscale permeability coefficient  $l = 0$  (left) and  $l = 3$  (right).

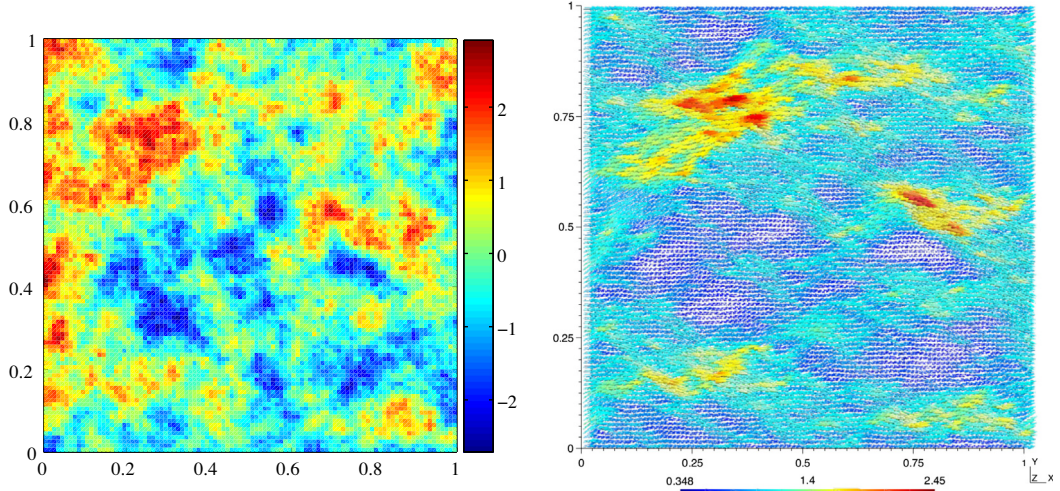


**Fig. 27.** The  $Y$  variable plot with constant values on squares (left), of which there are 100 along each axis of the unit square. The numerical velocity field (right) is computed using  $l = 2$  on triangles, of which there are two for each square of constant permeability.

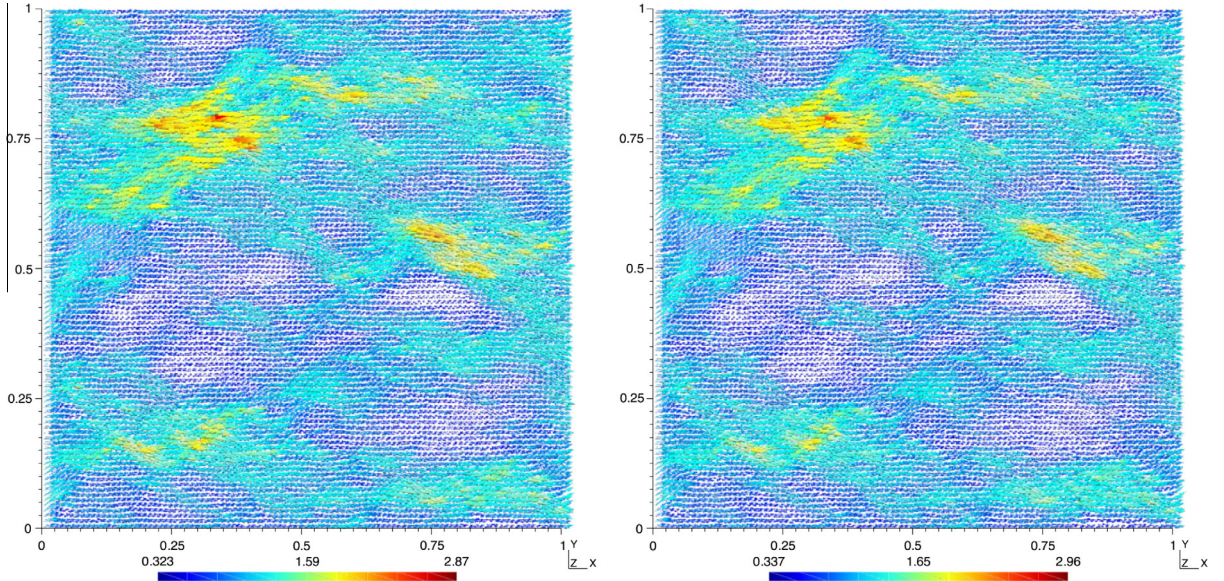


**Fig. 28.** Velocity fields computed using  $l = 2$  on a mesh with  $50 \times 50$  triangles (left) and  $25 \times 25$  triangles (right).

boundary conditions equal to one on the left and right edges and zero on top and bottom. We find the numerical solutions on a set of structured triangular meshes, taking  $l \in \{0, 2\}$  in the MHM method. The finest mesh consists of 100 triangular elements along each axis, the next mesh consists of 50, and finally the coarsest is composed of 25. On the finest mesh, the submesh used to numerically determine the basis functions on a given triangle is taken to be the triangle itself, whereas on the coarsest mesh, the submesh is set so that the union of the mesh and submeshes is the same as the finest mesh. The same holds for the mesh with 50 triangles along each axis. Fig. 26 shows sample basis functions resolved using a fine submesh on a triangle in the coarsest mesh. We can see the influence of multiscale coefficient on the design of the basis functions.

The first results consider the impact of high-order interpolation for the flux on the velocity fields using the finest mesh. This is shown in Figs. 27–29. In all cases, we see the velocity demonstrates the expected behavior, following closely the regions of higher permeability, but the case  $l = 2$  produces more marked incorporation of multiscale structures. Next, the coarser meshes are adopted in the case  $l = 2$ . Even though the velocity solution on the finest mesh is superior to those from coarser meshes, the performance on the coarsest is still quite good. We also see, on the coarsest mesh, a slight loss of detail for the case  $l = 0$  in relation to the method with  $l = 2$  (see Figs. 28 and 29). We conclude that, for practical purposes, the choice of adopting the coarsest mesh along with the MHM method with  $l = 0$  appears to be the better compromise between accuracy and computational cost.

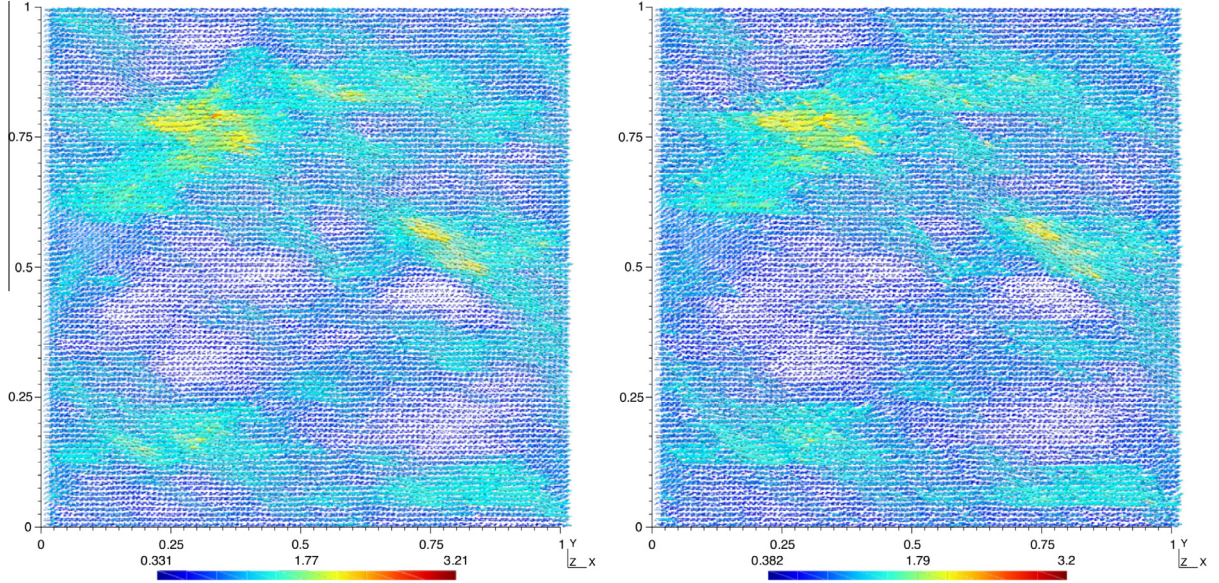


**Fig. 29.** Velocity fields computed using  $l = 0$  on a mesh with  $50 \times 50$  triangles (left) and  $25 \times 25$  triangles (right).

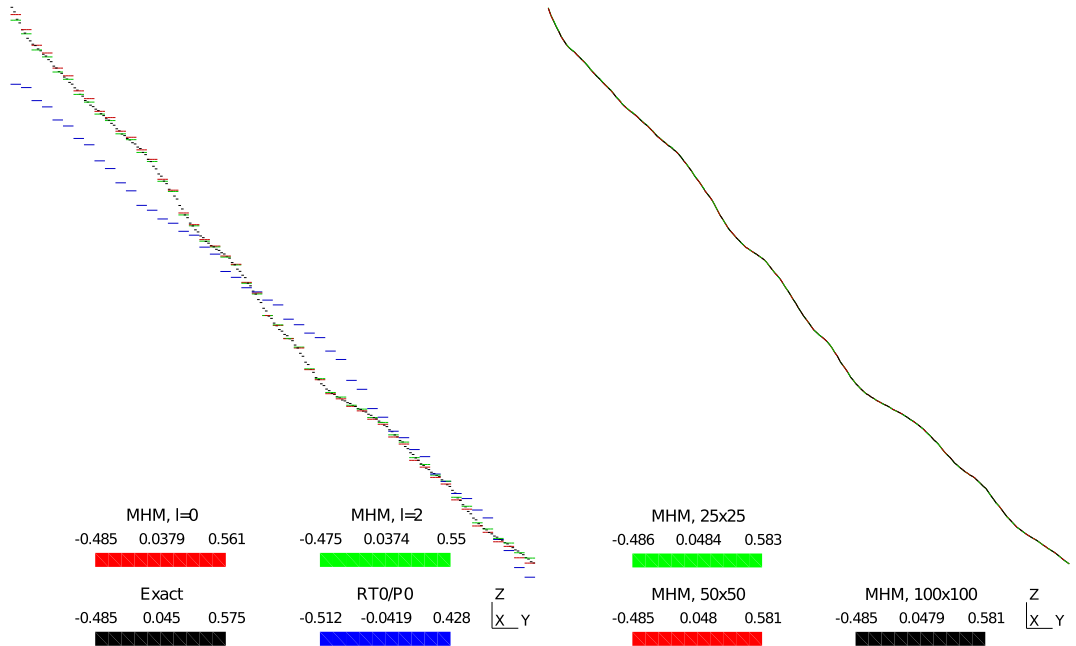


**Fig. 30.** Profiles of the pressure solutions. The left plot shows results from the lowest-order Raviart–Thomas method on the fine mesh with  $100 \times 100$  elements (fine mesh) (black) and on the mesh with  $25 \times 25$  elements (coarse mesh) (blue), and the MHM methods using  $l = 0$  (red) and  $l = 2$  (green) on the same coarse mesh. The right plot shows the results from the MHM methods with  $l = 2$  on the coarse (green) and fine (black) meshes, as well as on a mesh with  $50 \times 50$  elements (red). (For interpretation of the references to color in this figure legend, the reader is referred to the web version of this article.)

Next, we compare the methods on different meshes by considering the piecewise constant pressure in Fig. 30. The plots are obtained with a cut plane oriented vertically and containing the line from the lower right-hand to the upper left-hand corner of the domain. The left-hand plot shows that the results for  $p_0$  on the coarsest mesh for both  $l = 0$  and  $l = 2$  are in excellent accordance with the result obtained on the finest mesh using  $l = 0$ . Also shown is the result from the lowest-order Raviart–Thomas method on the coarsest mesh, which is clearly unacceptable. The right-hand plot shows  $p_0 + p^{l/2}$  obtained on each of the meshes have the same behavior.

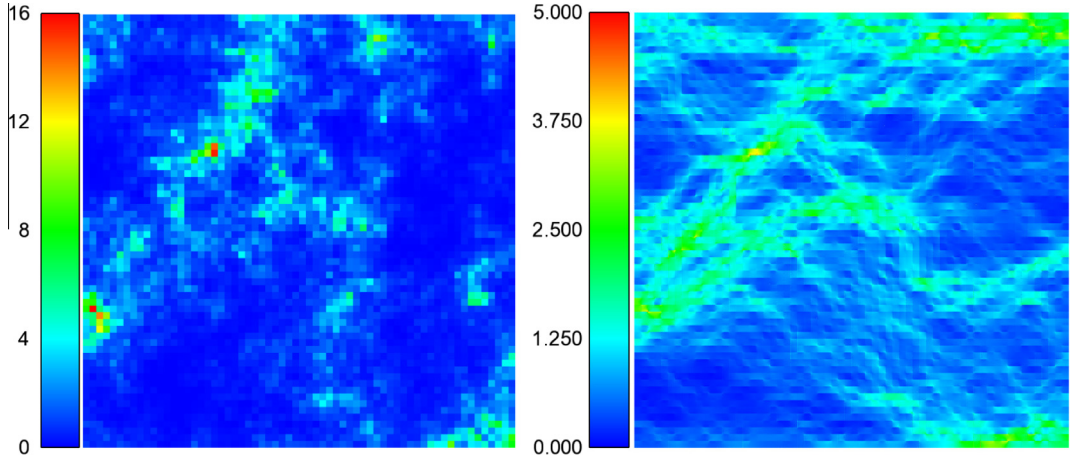


**Fig. 31.** Permeability field (left) and the absolute value of the velocity on the fine mesh (right).

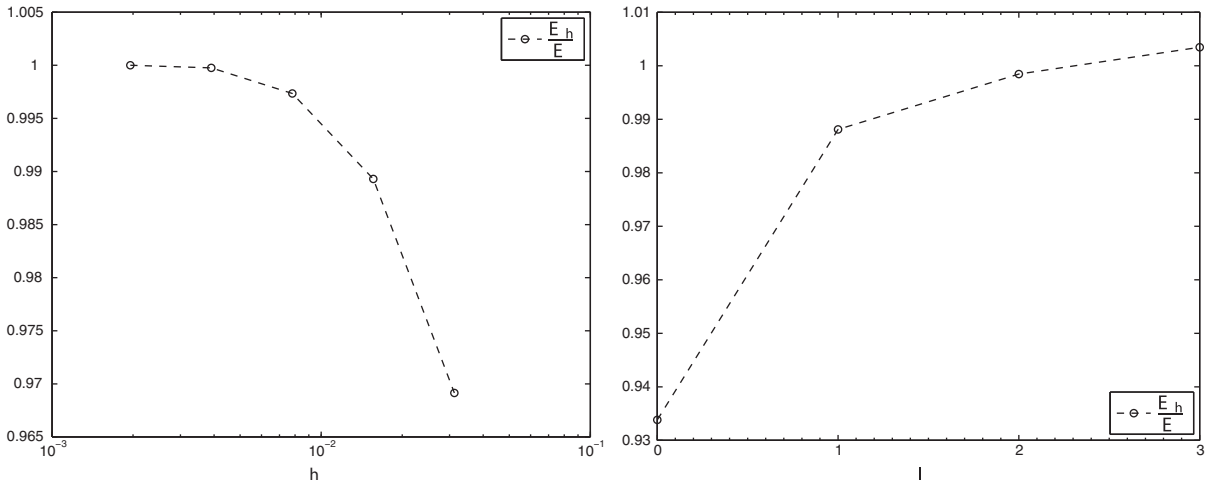


**Fig. 32.** Plot of  $\frac{E_h}{E}$  with respect to  $h$ -refinements (left) and increasing  $l$  (right).

It should be noted that these good results have been achieved by solving the local elliptic problems (25) and (26). Since previous tests suggest that using a mixed version of these problems, as pointed out in Remark 4, would likely lead to only a slight improvement, we decided not to explore this possibility here.

Finally, we produce a reference solution for a 2D log normal case (see Fig. 31) using a very fine mesh (around 2 millions of elements) to investigate whether MHM method on a coarse mesh is able to reproduce the dissipative energy due to viscous forces, i.e.,  $E := \frac{1}{2} \int_{\Omega} \mathcal{K} (\nabla p)^2$ . It is worth mentioning that an alternative way to compute the reference  $E$  may involve the concept of equivalent permeability of a heterogeneous medium (see [34,32] for an overview). Here, the reference quantity  $E$  is compared to its approximate counterpart  $E_h := \frac{1}{2} \int_{\Omega} \mathcal{K} (\nabla p_h)^2$ , where  $p_h$  is the solution of the MHM method on a coarse mesh. We find that  $\frac{E_h}{E}$  converges fast to 1 (see Fig. 32) with respect to both  $h$  refinement and increasing  $l$ .

We conclude that the MHM method preserves the dissipative energy quantity on coarse meshes with precision. Also, the investigation shows that, for a given target error  $\frac{E_h}{E}$ , it is computationally more attractive (in terms of total number of degrees of freedom) to increase  $l$  on a fixed coarse mesh than to use a low order  $l$  on a refined mesh.

## 6. Conclusion

This work proposes a new family of finite element methods for the Darcy equation, named Multiscale Hybrid-Mixed (MHM) methods, which accurately capture sub-scales. The MHM methods have been derived inside a space splitting strategy, resulting in basis functions which satisfy a Laplace equation in each element. The continuity of the solution is then enforced weakly using Lagrange multiplier, which has allowed the boundary conditions of the local problem to be set naturally. Numerical results demonstrate optimal convergence properties and a capacity to accurately incorporate heterogeneity and

high-contrast coefficients. In addition, the framework suggests a way to post-process the piecewise constant pressure and reconstruct a locally mass conservative velocity field such that the result is “super-close” to the exact solution with no extra computational cost. The MHM methods generalize in some sense other methods, such as the lowest-order Raviart–Thomas method, the mixed multiscale method [12], and the sub-grid upscaling method [4], and can further be interpreted as a stabilized primal hybrid method. In conclusion, the current family of methods emerges as an attractive alternative for solving mixed problems on complex geometries with high-order accuracy while taking advantage of high-performance parallel computation. Aspects related to the parallelization of the MHM algorithm as well as comparisons to well-rounded domain decomposition strategies as the FETI method [20] deserve deeper investigation as to highlight the exact value of the method to handle very large problems. Finally, its extension to advection-dominated problems may be performed within the same scope and is currently a work in progress in view of handling multiphase flows in porous media.

## Acknowledgments

The authors thank Marcio Borges and Leo Franca for a number of useful discussions which helped to improve the presentation of this paper. This work is dedicated to the memory of Leo Franca.

## References

- [1] A. Allendes, G.R. Barrenechea, E. Hernandez, F. Valentin, A two-level enriched finite element method for a mixed problem, *Math. Comput.* 80 (2011) 11–41.
- [2] R. Araya, C. Harder, D. Paredes, F. Valentin, Multiscale hybrid-mixed methods, LNCC Report No. 3/2013.
- [3] T. Arbogast, Analysis of a two-scale locally conservative subgrid upscaling for elliptic problems, *SIAM J. Numer. Anal.* 42 (2) (2004) 576–598.
- [4] T. Arbogast, K.J. Boyd, Subgrid upscaling and mixed multiscale finite elements, *SIAM J. Numer. Anal.* 44 (2006) 1150–1171.
- [5] D.N. Arnold, F. Brezzi, B. Cockburn, L.D. Marini, Unified analysis of discontinuous Galerkin methods for elliptic problems, *SIAM J. Numer. Anal.* 39 (2002) 1749–1779.
- [6] I. Babuska, E. Osborn, Generalized finite element methods: their performance and their relation to mixed methods, *SIAM J. Numer. Anal.* 20 (3) (1983) 510–536.
- [7] G.R. Barrenechea, L.P. Franca, F. Valentin, A Petrov–Galerkin enriched method: a mass conservative finite element method for the Darcy equation, *Comput. Methods Appl. Mech. Eng.* 196 (2) (2007) 2449–2464.
- [8] G.R. Barrenechea, L.P. Franca, F. Valentin, A symmetric nodal conservative finite element method for the Darcy equation, *SIAM J. Numer. Anal.* 47 (5) (2009) 3652–3677.
- [9] F. Brezzi, B. Cockburn, L.D. Marini, E. Suli, Stabilization mechanisms in discontinuous Galerkin finite element methods, *Comput. Methods Appl. Mech. Eng.* 195 (2006) 3293–3310.
- [10] F. Brezzi, M. Fortin, *Mixed and hybrid finite element methods*, Springer Series in Computational Mathematics, vol. 15, Springer-Verlag, Berlin, NY, 1991.
- [11] F. Brezzi, A. Russo, Choosing bubbles for advection–diffusion problems, *Math. Models Methods Appl. Sci.* 4 (4) (1994) 571–587.
- [12] Z. Chen, T.Y. Hou, A mixed multiscale finite element method for elliptic problems with oscillating coefficients, *Math. Comput.* 72 (242) (2002) 541–576.
- [13] Z. Chen, G. Huan, Y. Ma, *Computational Methods for Multiphase Flows in Porous Media*, SIAM Publication, Philadelphia, 2006.
- [14] C.C. Chu, I.G. Graham, T.Y. Hou, A new multiscale finite element method for high-contrast elliptic interfaces problems, *Math. Comput.* 79 (272) (2009) 1915–1955.
- [15] B. Cockburn, J. Gopalakrishnan, R. Lazarov, Unified hybridization of discontinuous Galerkin, mixed, and continuous Galerkin methods for second order elliptic problems, *SIAM J. Numer. Anal.* 47 (2) (2009) 1319–1365.
- [16] L. Demkowicz, J. Gopalakrishnan, Analysis of the DPG method for the Poisson equation, ICES Report 10-37, The University of Texas at Austin, 2010.
- [17] Y. Efendiev, J. Galvis, X.-H. Wu, Multiscale finite element methods for high-contrast problems using local spectral basis functions, *J. Comput. Phys.* 230 (4) (2011) 937–955.
- [18] A. Ern, J.-L. Guermond, *Theory and Practice of Finite Elements*, Springer-Verlag, Berlin, NY, 2004.
- [19] C. Farhat, I. Harari, L.P. Franca, The discontinuous enrichment method, *Comput. Methods Appl. Mech. Eng.* 190 (48) (2001) 6455–6479.
- [20] C. Farhat, J. Mandel, F.X. Roux, Optimal convergence properties of the FETI domain decomposition method, *Comput. Methods Appl. Mech. Eng.* 115 (1994) 367–388.
- [21] H. Fernando, C. Harder, D. Paredes, F. Valentin, Numerical multiscale methods for a reaction dominated model, *Comput. Methods Appl. Mech. Eng.* 201–204 (2012) 228–244.
- [22] L.P. Franca, C. Harder, F. Valentin, On a residual local projection method for the Darcy equation, *C.R. Acad. Sci. Paris* 347 (2009) 1105–1110.
- [23] L.P. Franca, A.L. Madureira, F. Valentin, Towards multiscale functions: enriching finite element spaces with local but not bubble-like functions, *Comput. Methods Appl. Mech. Eng.* 194 (2005) 3006–3021.
- [24] L.P. Franca, A. Russo, Deriving upwinding, mass lumping and selective reduced integration by residual-free bubbles, *Appl. Math. Lett.* 9 (5) (1996) 83–88.
- [25] T.Y. Hou, X. Wu, A multiscale finite element method for elliptic problems in composite materials and porous media, *J. Comput. Phys.* 134 (1) (1997) 169–189.
- [26] M. Murad, C. Moyne, A three-scale computational model of reactive pollutant transport in smectitic clays, *Commun. Numer. Methods Eng.* 22 (8) (2006) 875–891.
- [27] J.C. Nédélec, Mixed finite elements in  $R^3$ , *Numer. Math.* 35 (1980) 315–341.
- [28] T.H.H. Pian, Finite element formulation by variational principles with relaxed continuity requirements, in: A.K. Aziz (Ed.), *The Mathematical Foundations of the Finite Element Method with Applications to Partial Differential Equations*, Part II, vol. 49, Academic Press, New York, 1972, pp. 671–687.
- [29] T.H.H. Pian, P. Tong, Basis of finite element methods for solid continua, *Int. J. Numer. Methods Eng.* 1 (1) (1969) 3–28.
- [30] P.A. Raviart, J.M. Thomas, A mixed finite element method for 2nd order elliptic problems, *Mathematical Aspects of Finite Element Methods*, Lecture Notes in Mathematics, vol. 606, Springer-Verlag, New York, 1977.
- [31] P.A. Raviart, J.M. Thomas, Primal hybrid finite element methods for 2nd order elliptic equations, *Math. Comput.* 31 (138) (1977) 391–413.
- [32] P. Renard, G. de Marsily, Calculating equivalent permeability: a review, *Adv. Water Resour.* 20 (5–6) (1997) 253–278.
- [33] A. Riaz, H.A. Tchelepi, Dynamics of vertical displacement in porous media associated with CO<sub>2</sub> sequestration, *SPE J.* 13 (3) (2008) 305–313.
- [34] R.K. Romeu, B. Notinger, Calculation of internodal transmissibilities in finite-difference models of flow in heterogeneous media, *Water Resour. Res.* 31 (4) (1995) 943–959.
- [35] G. Sangalli, Capturing small scales in elliptic problems using a residual-free bubbles finite element method, *SIAM Multiscale Model. Simul.* 1 (3) (2003) 485–503.